Molecular Cell

Article

A Selective Autophagy Pathway for Phase-Separated Endocytic Protein Deposits

Graphical Abstract

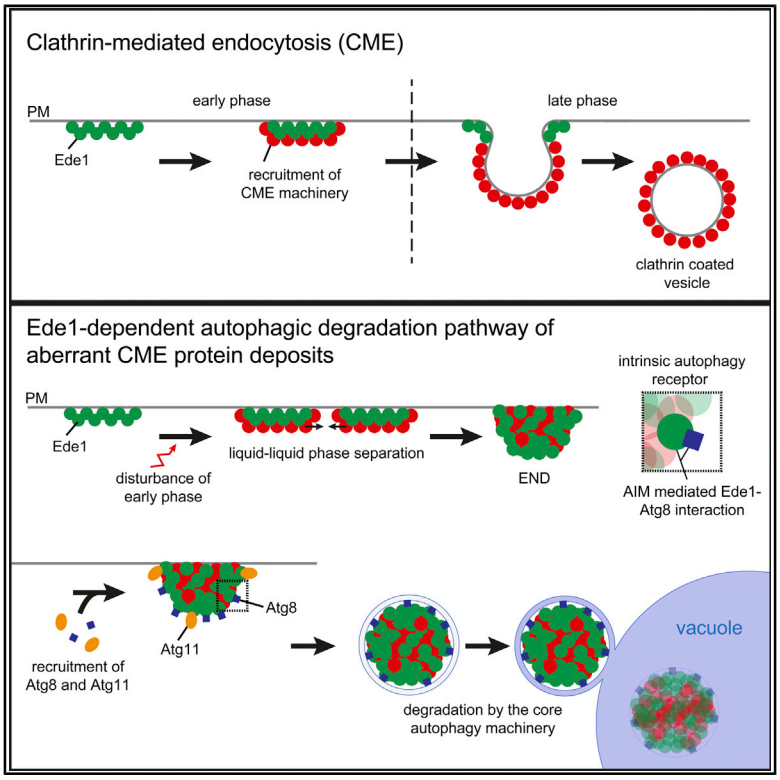

Highlights

- Ede1 is an intrinsic autophagy receptor for aberrant CME protein assemblies
- Aberrant CME assemblies form by liquid-liquid phase separation
- Liquid-liquid phase separation of Ede1 is important for autophagic degradation
- Ultrastructural view of an LLPS compartment at the PM and within autophagic bodies

Authors

Florian Wilfling, Chia-Wei Lee, Philipp S. Erdmann, ..., Boris Pfander, Brenda A. Schulman, Wolfgang Baumeister

Correspondence

fwilfling@biochem.mpg.de (F.W.), erdmann@biochem.mpg.de (P.S.E.), baumeist@biochem.mpg.de (W.B.)

In Brief

Removal of nonfunctional macromolecular complexes is important for cellular homeostasis. Wilfling et al. report a selective autophagy pathway for degradation of unproductive protein assemblies within the clathrin-mediated endocytosis machinery. The scaffold protein Ede1 hereby acts as a built-in quality control monitoring the assembly state of the clathrin-mediated endocytosis machinery.

Wilfling et al., 2020, Molecular Cell *80*, 764–778
December 3, 2020
https://doi.org/10.1016/j.molcel.2020.10.030

CellPress

CellPress
OPEN ACCESS

Molecular Cell

Article

A Selective Autophagy Pathway for Phase-Separated Endocytic Protein Deposits

Florian Wilfling,[1,2,6,7,9,*] Chia-Wei Lee,[1,2,7] Philipp S. Erdmann,[2,*] Yumei Zheng,[3,4] Dawafuti Sherpa,[6] Stefan Jentsch,[1,8] Boris Pfander,[5] Brenda A. Schulman,[3,6] and Wolfgang Baumeister[2,*]

[1]Molecular Cell Biology, Max Planck Institute of Biochemistry, 82152 Martinsried, Germany
[2]Molecular Structural Biology, Max Planck Institute of Biochemistry, 82152 Martinsried, Germany
[3]Department of Structural Biology, St. Jude Children's Research Hospital, Memphis, TN, USA
[4]Department of Microbiology, Immunology and Biochemistry, University of Tennessee Health Science Center, Memphis, TN, USA
[5]DNA Replication and Genome Integrity, Max Planck Institute of Biochemistry, 82152 Martinsried, Germany
[6]Molecular Machines and Signaling, Max Planck Institute of Biochemistry, 82152 Martinsried, Germany
[7]These authors contributed equally
[8]Deceased during the course of this study
[9]Lead Contact
*Correspondence: fwilfling@biochem.mpg.de (F.W.), erdmann@biochem.mpg.de (P.S.E.), baumeist@biochem.mpg.de (W.B.)
https://doi.org/10.1016/j.molcel.2020.10.030

SUMMARY

Autophagy eliminates cytoplasmic content selected by autophagy receptors, which link cargo to the membrane-bound autophagosomal ubiquitin-like protein Atg8/LC3. Here, we report a selective autophagy pathway for protein condensates formed by endocytic proteins in yeast. In this pathway, the endocytic protein Ede1 functions as a selective autophagy receptor. Distinct domains within Ede1 bind Atg8 and mediate phase separation into condensates. Both properties are necessary for an Ede1-dependent autophagy pathway for endocytic proteins, which differs from regular endocytosis and does not involve other known selective autophagy receptors but requires the core autophagy machinery. Cryo-electron tomography of Ede1-containing condensates, at the plasma membrane and in autophagic bodies, shows a phase-separated compartment at the beginning and end of the Ede1-mediated selective autophagy route. Our data suggest a model for autophagic degradation of macromolecular protein complexes by the action of intrinsic autophagy receptors.

INTRODUCTION

Macroautophagy, hereafter called autophagy, is a highly conserved and ubiquitous process that eliminates cytosolic components in response to starvation and cellular stresses. Cargoes destined for autophagic elimination are sequestered into a *de novo* synthesized double-membrane structure called autophagosome that fuses with the vacuole/lysosome for degradation (Dikic, 2017; Wen and Klionsky, 2016). Specific cargo is recruited to autophagosomes because of interaction with autophagy receptors, which often display Atg8-interacting motifs (AIMs) (Nakatogawa et al., 2009; Reggiori et al., 2012). AIM sequences in turn bind Atg8, a ubiquitin-like protein covalently linked to phosphatidylethanolamine (PE) in the isolation membrane (Farré and Subramani, 2016; Ohsumi, 2001). Thus, autophagy receptors couple their cargo to the autophagosome biogenesis pathway and allow packaging and subsequent disposal of a range of cytosolic entities.

Much of our understanding of selective autophagy is derived from matching receptors with important cargo, such as organelles, aggregates, or large macromolecular complexes (Behrends et al., 2010; Dikic and Elazar, 2018; Gatica et al., 2018). However, our knowledge of the molecular mechanisms underlying selective sequestration of autophagic cargo remains rudimentary. One of the best-studied examples is the mammalian autophagy receptor p62, which targets ubiquitylated misfolded proteins and phase separates into condensates through multivalent interactions established with multiple ubiquitins linked in chains (Jakobi et al., 2020; Sun et al., 2018; Zaffagnini et al., 2018). In addition, in the yeast cytoplasm-to-vacuole targeting (Cvt) pathway, the cargo forms condensates through phase separation (Yamasaki et al., 2020). In both cases, the autophagy receptor AIM sequences display relatively low affinity for Atg8, but concentration of cargo-receptor complexes before their enclosure facilitates avid interaction with multiple, membrane-linked Atg8 molecules (Johansen and Lamark, 2020; Kirkin and Rogov, 2019; Zaffagnini and Martens, 2016). These findings raise the possibility that liquid-liquid phase separation (LLPS) may generally contribute to receptor and cargo selection in selective autophagy pathways.

Here, using an unbiased approach to identify Atg8-interacting proteins, we report a previously undescribed autophagy pathway for phase-separated endocytic protein deposits.

Normally, proteins mediating clathrin-mediated endocytosis (CME) assemble and disassemble into complex protein and membrane machinery in a highly orchestrated manner to ultimately transport diverse cargo molecules from the cell surface to the interior (Lu et al., 2016; Merrifield and Kaksonen, 2014). In the early phase of CME, endocytic proteins and cargo accumulate at the PM, followed by invagination and scission of the vesicle during the late phase. Failure in the assembly, particularly during the early phase in which actin is not yet recruited, leads to clustering of unproductive endocytic protein assemblies with varying stability in both yeast and mammalian cells (Boeke et al., 2014; Kirchhausen et al., 2014; Mettlen et al., 2018). However, both the drivers of CME protein clustering during impaired endocytosis and the fate of these clusters remain unknown. We uncover an unexpected role of autophagy in the turnover of atypical deposits containing CME proteins. Our data suggest that the key early CME protein Ede1 has a dual role and functions as an autophagy receptor via AIM-dependent recruitment of Atg8 to sites of atypical CME protein assembly. We further characterize the material and structural properties of these endocytic protein deposits, describe molecular features of Ede1 contributing to deposit formation and degradation, and visualize their cellular structural properties from their beginning at the PM to their ultimate delivery to autophagosomes.

RESULTS

Quantitative Proteomics Identifies Atg8 Binding to CME Proteins

To identify novel autophagy receptors and cargo because of binding to Atg8, we performed label-free quantitative affinity-purification mass spectrometry (qMS) of GFP pull-downs from a yeast strain expressing N-terminally EGFP-tagged Atg8 and treated with rapamycin, a drug that activates the autophagy pathway by inactivating the TORC1 complex (Figure 1A; Noda and Ohsumi, 1998). 225 proteins were reproducibly and statistically significantly enriched between biological replicates (Figure S1A). Among those, the Atg8-conjugation machinery (Atg3, Atg4, and Atg7) and other proteins involved in autophagic processes, such as the Cvt pathway receptor Atg19, were identified. Our approach also revealed known autophagic cargo proteins such as Ape1, a target of the Cvt pathway, indicating that not only direct interactors of Atg8 but also receptor-cargo complexes were preserved (Figure 1B). Besides known autophagy cargoes, such as ribosomes and the nuclear pore complex, the Atg8 pull-down significantly enriched many proteins involved in the early steps of CME previously not known to bind Atg8 (Figures 1C, 1D, S1B, and S1C). In contrast, the actin machinery, which is recruited during the late phase of CME, was not enriched (Figure S1D).

Given that almost the complete early CME machinery was enriched in the Atg8 pull-downs, we hypothesized that at least one of these proteins might directly bind Atg8. To test this idea, we purified several recombinant clathrin coat assembly proteins that were present in our qMS experiment and incubated them *in vitro* with recombinant Atg8. Of these, only Ede1 directly bound Atg8 (Figure 1E). Coimmunoprecipitation (coIP) from yeast lysates confirmed the interaction of endogenously expressed Ede1 and Atg8, which was also observed in cells grown without addition of rapamycin, suggesting a nutrient-independent function (Figure 1F). Most known autophagy receptors not only bind Atg8 but also the scaffold protein Atg11 that is important to locally activate isolation membrane formation (Gatica et al., 2018; Kamber et al., 2015; Torggler et al., 2016; Yorimitsu and Klionsky, 2005). Indeed, we detected Ede1-Atg11 interaction by coIP, which depended on the fourth coiled-coil (CC) domain of Atg11 critical for recognizing phospho-activated receptor proteins (Figures 1G and S1E; Yorimitsu and Klionsky, 2005). Altogether, our data identify the early CME machinery as binding partners of Atg8 and point toward Ede1 as a potential autophagy receptor.

The Early Endocytic Protein Ede1 Recruits Atg8 Directly via AIM Interactions

Most known Atg8 binding proteins contain one or more AIMs that bind two adjacent hydrophobic pockets in Atg8 (Noda et al., 2010). To assess whether the Ede1-Atg8 interaction is AIM mediated, we used an Atg8 (Y49A, L50A) mutant impaired for binding in both sites and unable to bind AIM-containing proteins (Ho et al., 2009). The mutations disrupted the Ede1-Atg8 interaction, supporting the idea that Ede1 is an AIM-dependent receptor for Atg8 (Figure 2A). Computational prediction of potential AIMs and C-terminal truncation analysis identified the last three predicted AIMs as essential for interaction with Atg8, because their deletion abolished EGFP-Ede1 binding to glutathione S-transferase (GST)-Atg8, whereas deletion of the C-terminal ubiquitin-associated (UBA) domain alone had no effect (Figure 2B). AIM2 and AIM3 are conserved among different yeast species and are located in a large intrinsically disordered region (Figures S2A and S2B), a feature typical of most validated AIMs (Popelka and Klionsky, 2015). Peptide binding assays confirmed that the individual Ede1 AIMs are sufficient to bind Atg8 (Figure S2C). To test roles of individual AIMs, we expressed and purified GST-Ede1 constructs with all possible combinations of AIMs inactivated by alanine replacements and checked binding to recombinant Atg8. Mutations in AIM2 ($Ede1^{AIM2}$) strongly impaired the interaction (Figure 2C). Double mutation of AIM2 and AIM3 ($Ede1^{AIM2+3}$) further reduced binding (Figure S2D), which was lost when all putative AIM motifs were mutated ($Ede1^{AIMR}$) (Figure 2C). As control, mutations in the Eps15-homology (EH) domains ($Ede1^{EH\ 3W\text{-}A}$) (Dores et al., 2010), had no influence on the binding between Atg8 and Ede1 (Figure 2C).

To determine the structural basis for the Atg8-Ede1 interaction, we pursued a crystal structure of Atg8 in complex with Ede1 fragments. Crystals were obtained with an Ede1 peptide containing AIM1 and AIM2 (Figure 2D; Table 1). A high-resolution structure showed that AIM1 folds within a short helix, and the aromatic Phe1238 and the hydrophobic Ile1241 of AIM2 engages the W-site and L-site of Atg8, respectively, whereas the negatively charged Asp1242 forms ionic interactions with Arg28, resembling other known classical AIM-Atg8 interactions (Kirkin and Rogov, 2019). Ede1 harbors additional Atg8 binding elements, including a few acidic residues upstream and a helix downstream of AIM2 (Figure S2E). Similar interactions were observed previously between a mammalian GABARAP Atg8 ortholog and ankyrin protein, in which the pre-LIR (LC3-interacting region) acidic side chains and a post-LIR helix stabilized the complex (Figure S2F; Li et al., 2018). The dissociation constant

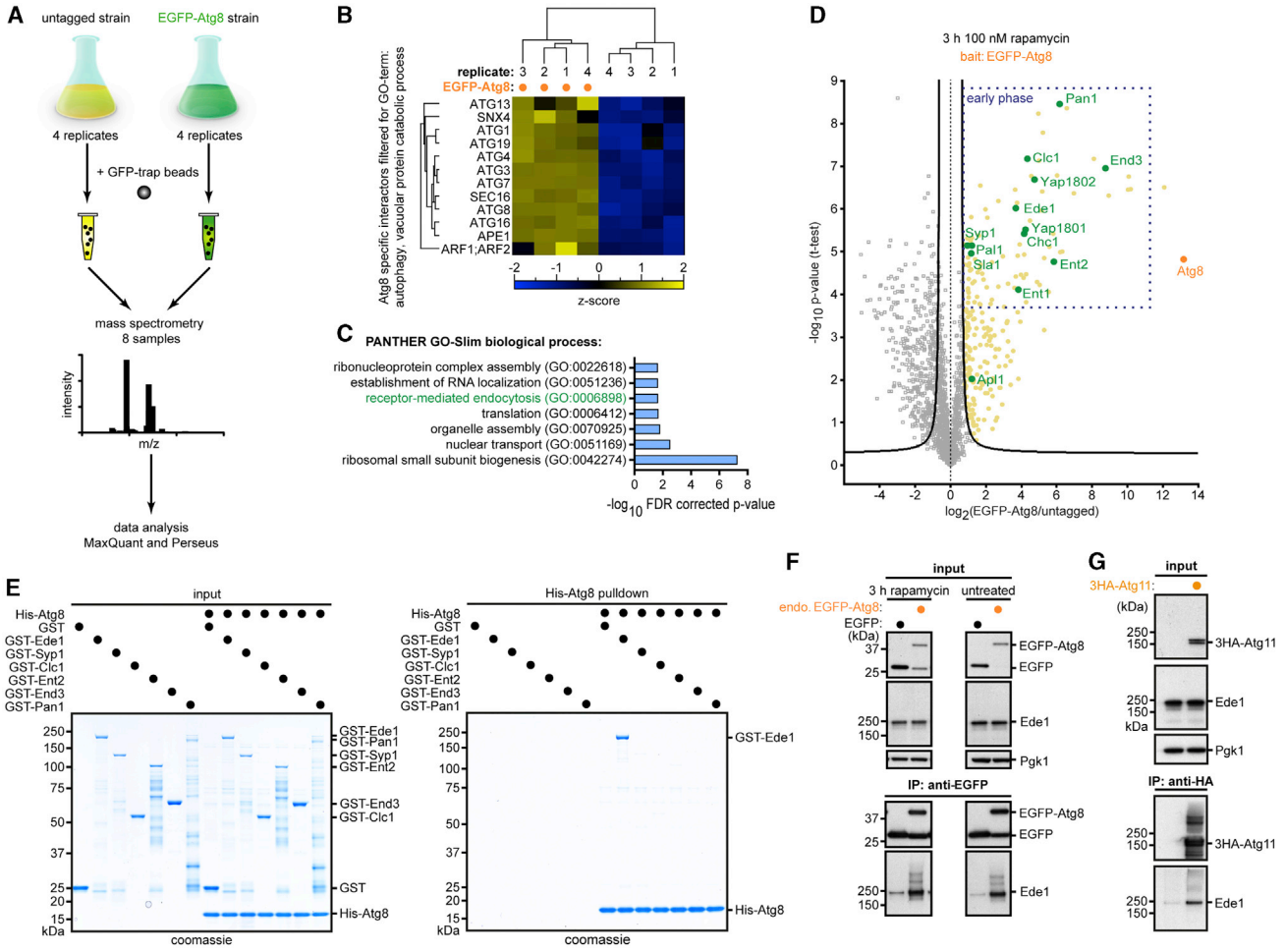

Figure 1. Quantitative Proteomics Identifies the Early CME Machinery as Atg8 Binders

(A) Workflow for immunoprecipitation-mass spectrometry (IP-MS) analysis of cells expressing EGFP-Atg8 under the control of the *ADH* promoter (p*ADH*) after induction of autophagy with rapamycin.

(B and C) Gene Ontology (GO) term categories of proteins enriched in the EGFP-Atg8 pull-down (PD). Significant EGFP-Atg8 interactors were filtered for the autophagy and vacuolar protein catabolic process (B) or for biological processes (C). Matching ANOVA-positive and false discovery rate (FDR)-corrected hits are displayed by hierarchical clustering of the respective *Z* scores for each sample (B).

(D) Volcano plot representing Atg8-interacting proteins. The hyperbolic curve separates specifically interacting proteins (yellow) from the background (gray) (FDR: 0.05, S0: 1.0). EGFP-Atg8 interactors involved in CME are marked in green; EGFP-Atg8 is in orange. The dark blue box indicates proteins involved in the early phase of endocytosis.

(E) Ni-NTA PD of recombinant His-Atg8 (8 nM) with different recombinant GST-tagged endocytic machinery proteins (0.8 nM each), including Ede1, Syp1, Clc1, Ent2, End3, or Pan1.

(F) Validation of Ede1-Atg8 interaction by coIP of EGFP-Atg8 expressed under the endogenous promoter with or without rapamycin treatment. A strain expressing EGFP under the Atg8 promoter serves as control. Pgk1 serves as loading control.

(G) Atg11 (p*ADH*) was 3 hemagglutinin (3HA) epitope tagged, and its interaction with Ede1 was probed by coIP and immunoblotting with anti-Ede1 antibody. See also Figure S1.

(K_D) for the Ede1-Atg8 interaction was measured in the low micromolar range (Figure S2G), which is similar to that of other known autophagy receptors but differs from ankyrin (Johansen and Lamark, 2020; Kirkin and Rogov, 2019).

Ede1 Is Necessary for Atg8 Binding to Aberrant CME Protein Deposits

To ascertain whether Ede1 displays properties of an autophagy receptor, we introduced the *ede1*^{AIMR} mutant into the endogenous *EDE1* locus. EGFP-Atg8 coIP confirmed that Atg8 binding to Ede1 *in vivo* depends on its AIMs. In contrast, *ede1*^{AIMR} did not affect Atg8 recruitment of Ape1, and deletion of *APE1* did not affect the interaction between Ede1 and Atg8 (Figure 3A). Moreover, mutating the AIMs in Ede1 had no effect on the rate of autophagosome biogenesis, bulk autophagy, or other selective autophagy pathways examined (Figures S2H–S2L). To unbiasedly identify potential Ede1 cargo, we compared by qMS the EGFP-Atg8 interactome of wild-type (WT) and *ede1*^{AIMR} mutant

CellPress
OPEN ACCESS

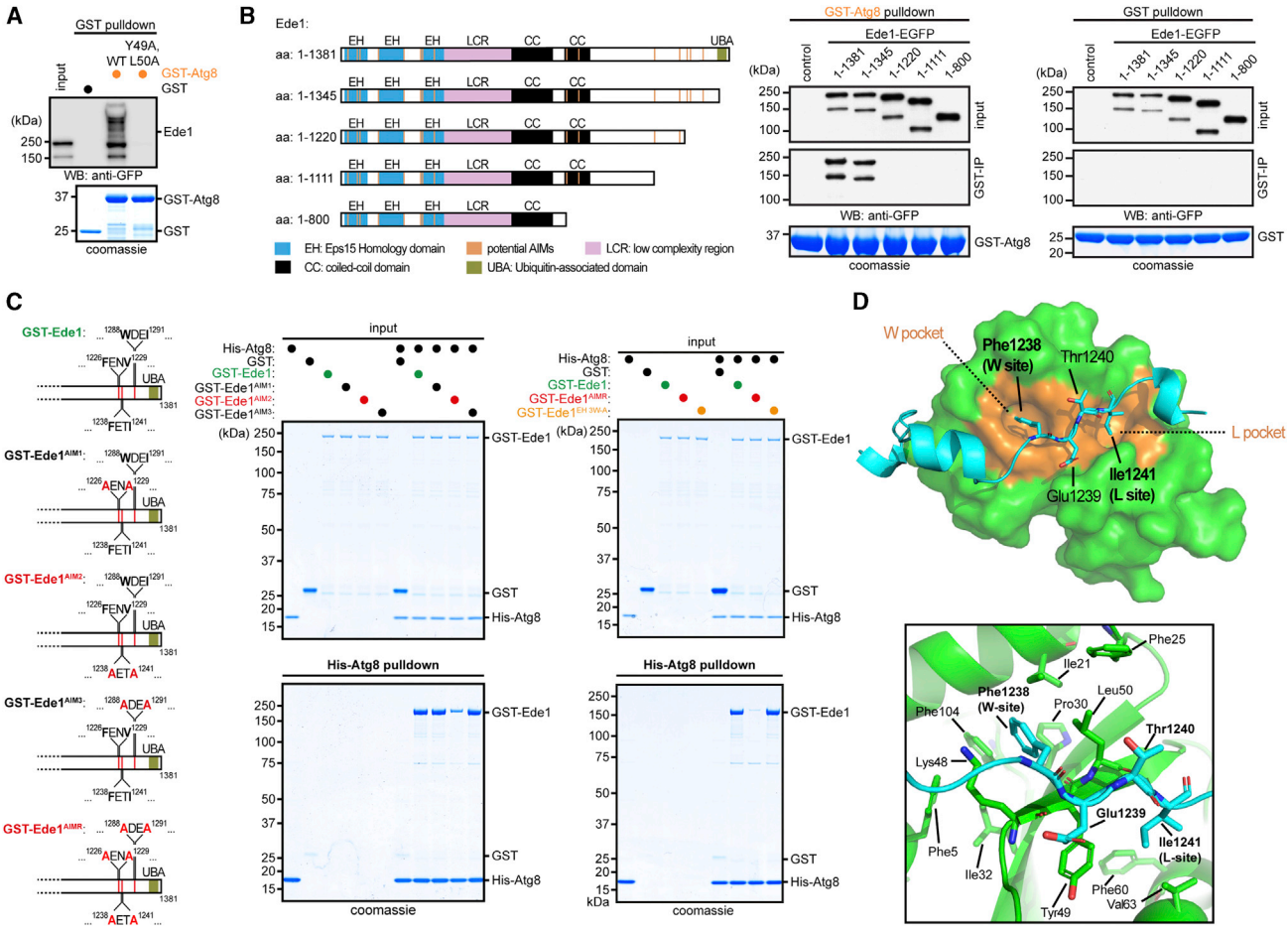

Figure 2. Ede1 Recruits Atg8 Directly via Classical AIM Interactions

(A) Lysates from WT cells were incubated with recombinant His-Atg8 or the Y49A, L50A mutant, followed by Ni-NTA PD and immunoblotting with anti-Ede1 antibody.

(B) Cell lysates expressing different EGFP-tagged Ede1 C-terminal deletion mutants were incubated with recombinant GST-Atg8 or GST alone, followed by GST PD and immunoblotting with anti-GFP antibody. The illustration shows truncation mutants used to map the Atg8 binding site. EH, Eps15 homology; CC, coiled coil; UBA, ubiquitin associated; aa, amino acid.

(C) Ni-NTA PD of recombinant His-Atg8 (8 nM) with GST-Ede1 WT, single AIM mutants (Ede1^{AIM1}, Ede1^{AIM2}, or Ede1^{AIM3}) (left), or a triple AIM mutant (Ede1^{AIMR}) (0.8 nM each) (right). Ede1$^{EH\ 3W\text{-}A}$ mutant defective in NPF-tripeptide binding was used as control. The schematic shows position of the different AIM mutants.

(D) Crystal structure of Ede1(1,220–1,247) peptide bound to Atg8, showing Ede1 Phe1238 and Ile1241 in Atg8 W and L pockets, respectively (top). AIM2 binding to Atg8 is achieved by hydrophobic interactions among its W/L-sites of Atg8 (bottom).

See also Figure S2.

cells. Analysis revealed that in particular, PM-localized proteins were enriched in an Ede1-dependent manner (Figures S3A–S3C). Among those, many endocytic proteins involved in the early stages of CME could be seen and confirmed in multiple cases (Figures 3B and S3D).

To gain insights into functional roles of Ede1-Atg8 interactions, we fluorescently tagged both proteins and performed live-cell imaging. Atg8 showed colocalization in ~5% of cells at sites of strong Ede1 accumulation (Figure 3C). These Ede1 clusters coexist but differ from typical endocytic patches, because they strongly and stably accumulate Ede1, as revealed by time-lapse microscopy (Figure 3D). To exclusively monitor sites of Ede1-Atg8 interaction, we turned to a bimolecular fluorescence complementation (BiFC) strategy by tagging both proteins with either the N-terminal Venus (VN) or the C-terminal Venus (VC) fragment. A fluorescent BiFC signal was observed at a few sites close to the PM, which was lost in *ede1^{AIMR}* mutant cells, although protein levels were comparable (Figures S4A and S4B). Moreover, mars-tagged Chc1, Syp1, Sla2, End3, and Pan1 all colocalized at Ede1-Atg8 BiFC foci, suggesting that these are the sites at which Ede1 mediates the binding of endocytic proteins to Atg8 (Figure S4C).

These aberrant Ede1 clusters, which sporadically occurred in proliferating WT cells, resembled those reported to accumulate when Ede1 is overexpressed or when a specific combination of early endocytosis adaptor proteins is deleted (*yap1801*Δ, *yap1802*Δ, and *apl3*Δ, hereafter called ΔΔΔ) (Boeke et al., 2014). To compare them to the ones observed in WT cells, we

Table 1. Crystallography Data Collection and Refinement, Related to Figure 2D

	ScEde1 (1,220–1,247)-ScAtg8 (1–116)
Data Collection	
Space grouph	$P4_3$
Cell Dimensions	
a, b, c (Å)	49.642, 49.642, 123.446
α, β, γ (°)	90, 90, 90
Wavelength (Å)	0.979
Resolution (Å)[a]	46.06–1.773 (1.836–1.773)
R_{sym} or R_{merg}[a]	0.054 (0.060)
I/σ (I)[a]	29.36 (4.62)
CC½[a]	0.996 (0.862)
Completeness (%)[a]	99.97 (99.65)
Wilson B factor (Å^2)	24.92
Redundancy[a]	8.8 (7.6)
Refinement	
Resolution (Å)	46.06–1.773
No. reflections	28,859
R_{work}[a]	0.1756 (0.2240)
R_{free}[a]	0.2028 (0.2676)
Completeness (%)	99.94
No. atoms	2,421
Protein	2,205
Water	216
B factors (Å^2)	28.90
Protein	28.20
Solvent	36.60
RMSD	
Bond lengths (Å)	0.008
Bond angles (°)	1.17
Ramachandran plot	
Favored (%)	98
Outliers (%)	0
Clashscore	2.72

RMSD, root-mean-square deviation.
[a]Values in parentheses are for the highest-resolution shell.

performed time-lapse microscopy of EGFP-tagged Ede1 in ΔΔΔ mutant or Ede1-overexpressing cells. Similar to WT, those Ede1 clusters were stable and persisted for the duration of the experiments (Figure 3E). Moreover, both strains displayed an enhanced accumulation of other CME proteins at these stable, non-endocytic foci (Figures 3F and S4D). In contrast, late-phase proteins important for the scission step were excluded from these clusters (Figure S4E). Ede1 clustering was independent of EGFP tagging, because cells overexpressing untagged Ede1 showed still aberrant accumulation of Sla2- or Pan1-TagGFP2 (Figure S4F). To explore whether Ede1 recruits Atg8 to sites of aberrant CME assembly in ΔΔΔ mutant or Ede1-overexpressing cells, we monitored fluorescently tagged Atg8 and Ede1. Colocalization was exclusively observed at sites of aberrant Ede1 clustering and depended on the AIM region in Ede1, because Atg8 failed to colocalize with Ede1 clusters in *ede1*^{AIMR} mutant cells (Figures 3G and S4G). This colocalization, as well as the Ede1-Atg8 interaction, was significantly increased compared with WT cells, suggesting that impaired early CME assembly triggers Atg8 recruitment (Figures 3H and S4H).

Altogether, the data show (1) Ede1 corecruits early CME proteins to Atg8, (2) sites of their colocalization do not display normal endocytic mobility, and (3) they accumulate in yeast impaired for endocytosis. We refer hereafter to these atypical Ede1 clusters as Ede1-dependent endocytic protein deposits (ENDs), which have similar properties and composition in WT and mutant cells but are increased when endocytosis is impaired.

Ede1 and the Core Autophagy Machinery Are Necessary for Autophagic Degradation of END

Given that Atg8 is a constituent of the END assemblies, we hypothesized a role for autophagy. To explore this, we used the EGFP fusion assay, in which free EGFP (EGFP′) persists after degradation of the fusion partner in the vacuole (Shintani and Klionsky, 2004). To allow monitoring of EGFP cleavage under conditions of proliferative growth in rich nutrients, we performed GFP-trap pull-downs followed by western blot analysis of endogenously expressed EGFP-Ede1 strains (Figure 4A). This led to enrichment of EGFP′, which depended on both Atg8 and Ede1 AIMs, indicating that some EGFP-Ede1 is constitutively subjected to autophagic degradation (Figures 4B and 4C). This autophagic degradation of Ede1, as monitored by EGFP′, was enhanced by mutations impairing CME, such as the ΔΔΔ strain or knockout of clathrin light chain (*clc1*Δ) known to cause persistent patch formation of early CME proteins (Carroll et al., 2012; Figures 4B and S5A). Moreover, Ede1-dependent EGFP′ accumulation in the ΔΔΔ strain was observed for endogenously expressed CME-EGFP fusion proteins (Chc1-, Sla2-, or Pan1-EGFP) of END constituents, suggesting that Ede1-Atg8 interaction is a determinant of END degradation (Figure 4D).

Selective engulfment of autophagic cargo under rich conditions requires local isolation membrane formation, which is initiated by receptor-mediated recruitment of the autophagic scaffold protein Atg11 (Kamber et al., 2015; Torggler et al., 2016; Turco et al., 2019; Yorimitsu and Klionsky, 2005). Deletion of *ATG11* abolished enrichment of EGFP′, raising the possibility of phagophore assembly at sites of Ede1 accumulation (Figure 4E). Conversely, Atg19 or Cue5, autophagy receptors for the Cvt pathway or for degradation of ubiquitylated protein aggregates, showed no effect on EGFP′ enrichment (Figures 4E and S5B). Moreover, we observed interaction of Atg11 and Ede1 *in vivo* by BiFC and site-specific biotinylation assays (Figures S5C and S5D). In addition, RFP-Atg8 colocalized with sites of Atg11-Ede1 interaction, indicating the recruitment of the core autophagy machinery to END (Figure S5E). Autophagic bodies are preserved within the vacuole upon deletion of the vacuolar lipase *ATG15* (Epple et al., 2001). Under rich conditions, focal accumulation of EGFP-Ede1 in the vacuole was observed in a small percentage of *atg15*Δ cells (Figure 4F). The fraction of such cells increased when cells entered early stationary phase at which TORC1 activity is naturally reduced, in accordance with enhanced autophagic degradation of

CellPress
OPEN ACCESS

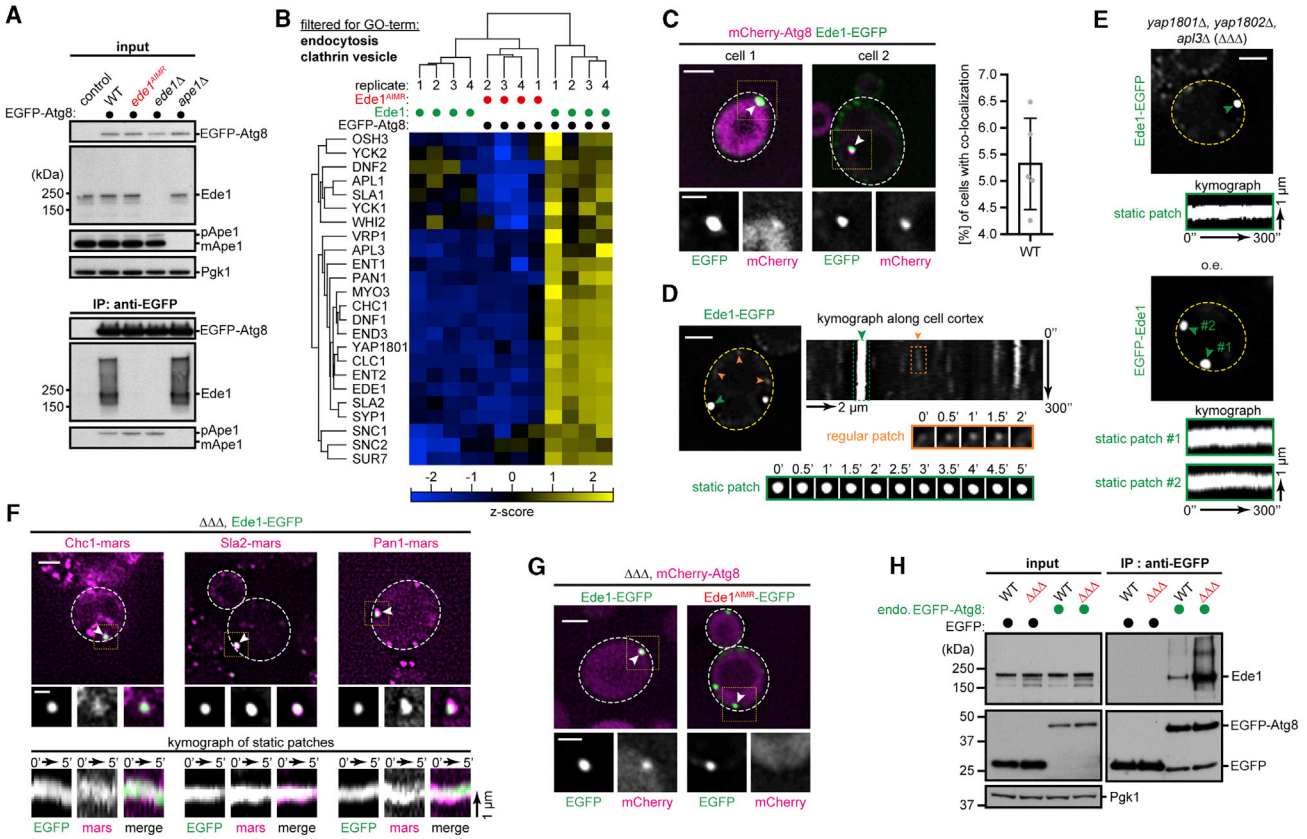

Figure 3. Ede1 Serves as a Receptor for Atypical CME Assemblies

(A) AIM-dependent binding of Ede1 to Atg8 in WT, Ede1^{AIMR}-mutated, *ede1*Δ, or *ape1*Δ cells after rapamycin treatment by coIP of EGFP-Atg8 (p*ADH*) and immunoblotting with the respective antibodies.

(B) Hierarchical cluster analysis filtered for the GO term endocytosis for all Ede1-dependent EGFP-Atg8 (p*ADH*) interactors identified by qMS (Figure S3A, red box).

(C) mCherry-Atg8 (p*ADH*) and EGFP-Ede1 colocalize at distinct sites of Ede1 clustering in a subset of WT cells. Quantification was performed for at least 500 cells (n = 5, mean ± SD).

(D) EGFP-Ede1 forms stable accumulations in a subpopulation of WT cells, which are distinct from regular endocytic patches (left). Kymograph representation of a movie (1 frame/5 s) of cells expressing EGFP-Ede1 (right). Orange arrows and boxes highlight regular endocytic Ede1 patches; green highlights atypical Ede1 clusters.

(E) Atypical stable accumulations of Ede1 are detected particularly in early-phase endocytic mutants; as in (D), but with deleted endocytic adopter proteins (*yap1801*Δ, *yap1802*Δ, *apl3*Δ; hereafter ΔΔΔ) (top) or cells overexpressing of Ede1 (p*ADH*) (bottom).

(F) CME proteins Chc1, Sla2, and Pan1 stably colocalize at sites of EGFP-Ede1 clustering in ΔΔΔ cells. Kymograph representation of a two-color movie (1 frame/20 s) of cells expressing EGFP-Ede1 and either Chc1-mars, Sla2-mars, or Pan1-mars in the ΔΔΔ background.

(G) Colocalization experiments between mCherry-Atg8 (p*ADH*) and EGFP-Ede1 or Ede1^{AIMR}-EGFP in the ΔΔΔ background.

(H) CoIP of EGFP-Atg8 (endogenous promoter) followed by western blot (WB) in WT and ΔΔΔ cells. Strains expressing EGFP under the Atg8 promoter serve as control.

For all fluorescence images, the scale bar represents 2 or 1 µm for inlets. See also Figures S3 and S4.

receptor-cargo complexes when the TORC1 kinase complex is inactivated (Kim et al., 2001; Lu et al., 2014; Mochida et al., 2015). In line, degradation of Ede1 and its partner early CME proteins was strongly enhanced when bulk autophagy was induced (Figures S5F and S5G). To explore at a systemwide level which proteins are involved in END degradation, we performed a high-content microscopy screen by crossing an EGFP-Ede1 overexpression strain against a deletion library of nonessential single-yeast gene knockouts. Analysis of Ede1 clusters before and after nitrogen starvation revealed 100 proteins (Z score > 1.5) defective in END degradation, most belonging to the core autophagy machinery, ESCRT, and a set of proteins mediating vacuolar docking and fusion (Figure 4G; Table S1). Detailed analysis of the autophagy pathway revealed a strong dependency on the core autophagy machinery. Notably, Atg11 contributes to, but is not essential for, degradation of END under bulk autophagy (Figures 4G and S5H), which is consistent with its reported role in selective autophagy (Kim et al., 2001; Matscheko et al., 2019). Single deletions of other known autophagy receptors, as well as proteins important for proteasomal degradation, did not affect degradation of END during nitrogen starvation (Figure 4G). Altogether,

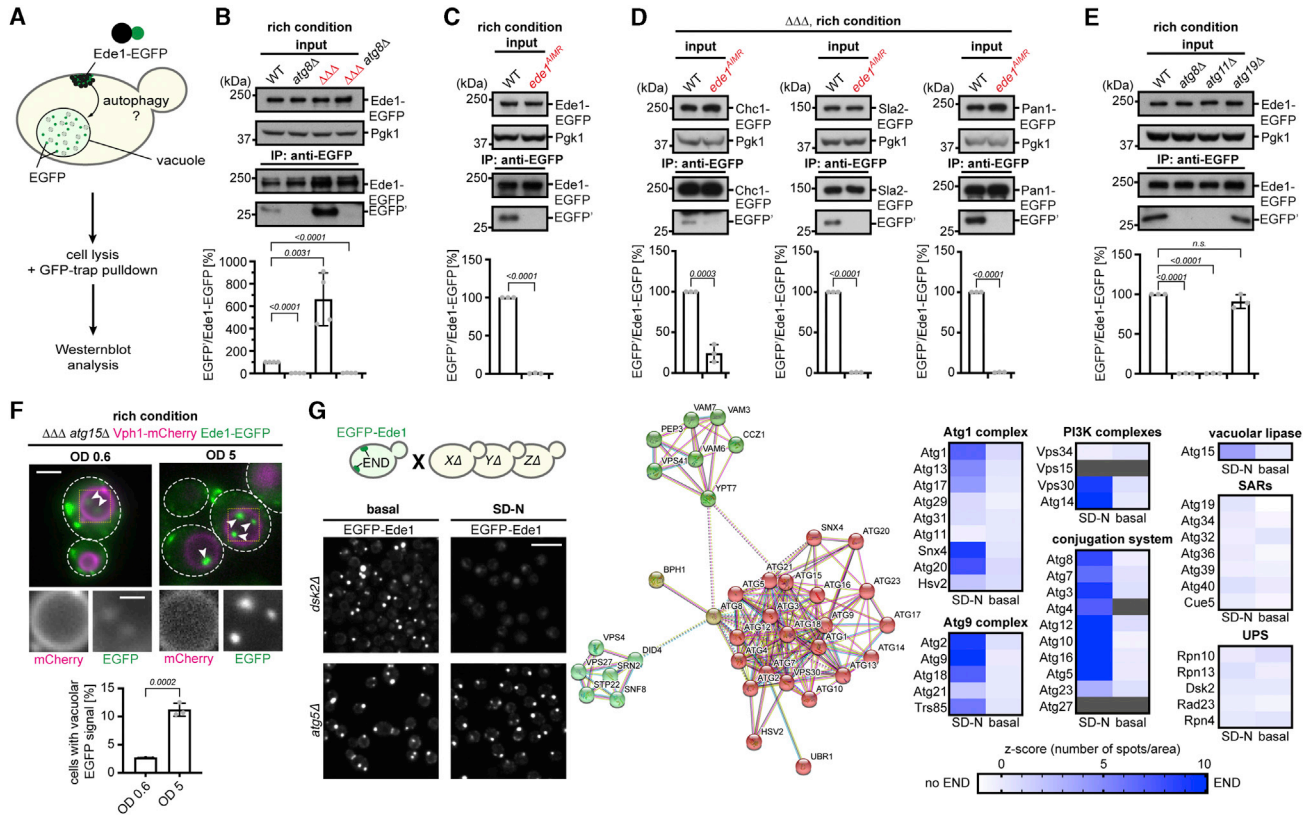

Figure 4. Ede1-Dependent Degradation of Aberrant CME Assemblies by the Core Autophagy Machinery

(A) Workflow for monitoring endogenously expressed EGFP-Ede1 cleavage during logarithmic cell growth in a rich medium. Cell lysates are subjected to coIP using GFP-trap resin. Both full-length EGFP-Ede1 and free EGFP (EGFP′) are monitored by WB analysis.

(B and C) Experimental setup as in (A), with *atg8*Δ, ΔΔΔ, and ΔΔΔ *atg8*Δ cells (B) or *ede1*^{AIMR} cells (C) compared with WT cells.

(D) Chc1, Sla2, or Pan1 were C-terminally EGFP tagged in ΔΔΔ cells with endogenous expression of Ede1 or Ede1^{AIMR}, and EGFP′ was detected by GFP-trap PD and immunoblotting as in (A).

(E) Autophagic turnover of Ede1 depends on Atg11 but is unaffected by Atg19; experimental setup as in (A), with *atg8*Δ, *atg11*Δ, and *atg19*Δ mutant cells.

(F) Focus-like accumulation of EGFP-Ede1 in the vacuole (Vph1-mars) is observed in ΔΔΔ *atg15*Δ cells (white arrows) at logarithmic or early stationary growth. Quantification shows the percentage of cells with a vacuolar EGFP-Ede1 signal, and data are mean ± SD of n = 3 independent experiments. Scale bars, 2 μm; inset, 1 μm.

(G) EGFP-Ede1 was crossed against a single-gene knockout library. Cells were fluorescent imaged under rich condition and after 24 h of nitrogen starvation. Protein hits from the screen were subjected to STRING analysis (middle) or a heatmap representation of selected gene knockouts (right). Scale bar, 15 μm.

Data for all WB quantifications show the ratio between EGFP′ and full-length EGFP fusion protein and are mean ± SD of n ≥ 3 independent experiments. Statistical analysis was performed using two-tailed Student's t tests; p values are indicated. Pgk1 serves as loading control for the input. See also Figure S5.

the results indicate that END is selectively degraded in an Ede1-dependent manner by the core autophagy machinery.

ENDs Exhibit Hallmarks of LLPS

Cargoes of selective autophagy are often discrete entities—membrane-encased organelles in mitophagy or endoplasmic reticulum (ER)-phagy or encapsulated pathogenic microbes in xenophagy—or, the in case of proteins, either specific structural assemblies (e.g., Cvt, proteophagy, or ferritinophagy) or assemblies with particular material properties (aggrephagy). To characterize material properties of END, we examined mobility of Ede1 within these clusters using fluorescence recovery after photobleaching (FRAP). FRAP experiments with EGFP-Ede1 showed (1) Ede1 moves dynamically within END, with a halftime of 1.87 ± 0.76 s (Figures 5A and S6A); (2) the END-located Ede1 pool exchanges with the cytosol, because prolonged bleaching of the cytoplasm led to a decrease of EGFP fluorescence within END (Figure S6B); and (3) in most cases, Ede1 does not form insoluble protein aggregates, because Hsp104-mars, a marker for cytosolic protein aggregation in yeast (Inoue et al., 2004; Shorter and Lindquist, 2004), is absent from sites of Ede1 accumulation (Figure 5B).

Weak multivalent interactions between networks of proteins, as found for the endocytic machinery (Smith et al., 2017), often drive LLPS of proteins (Banani et al., 2017; Harmon et al., 2017; Martin and Mittag, 2018). To examine whether such interactions lead to Ede1 condensation, we treated cells with hexanediol, an aliphatic alcohol that reversibly dissolves liquid-like assemblies in living cells (Alberti et al., 2019). Single-cell experiments using a microfluidic device allowed us to track

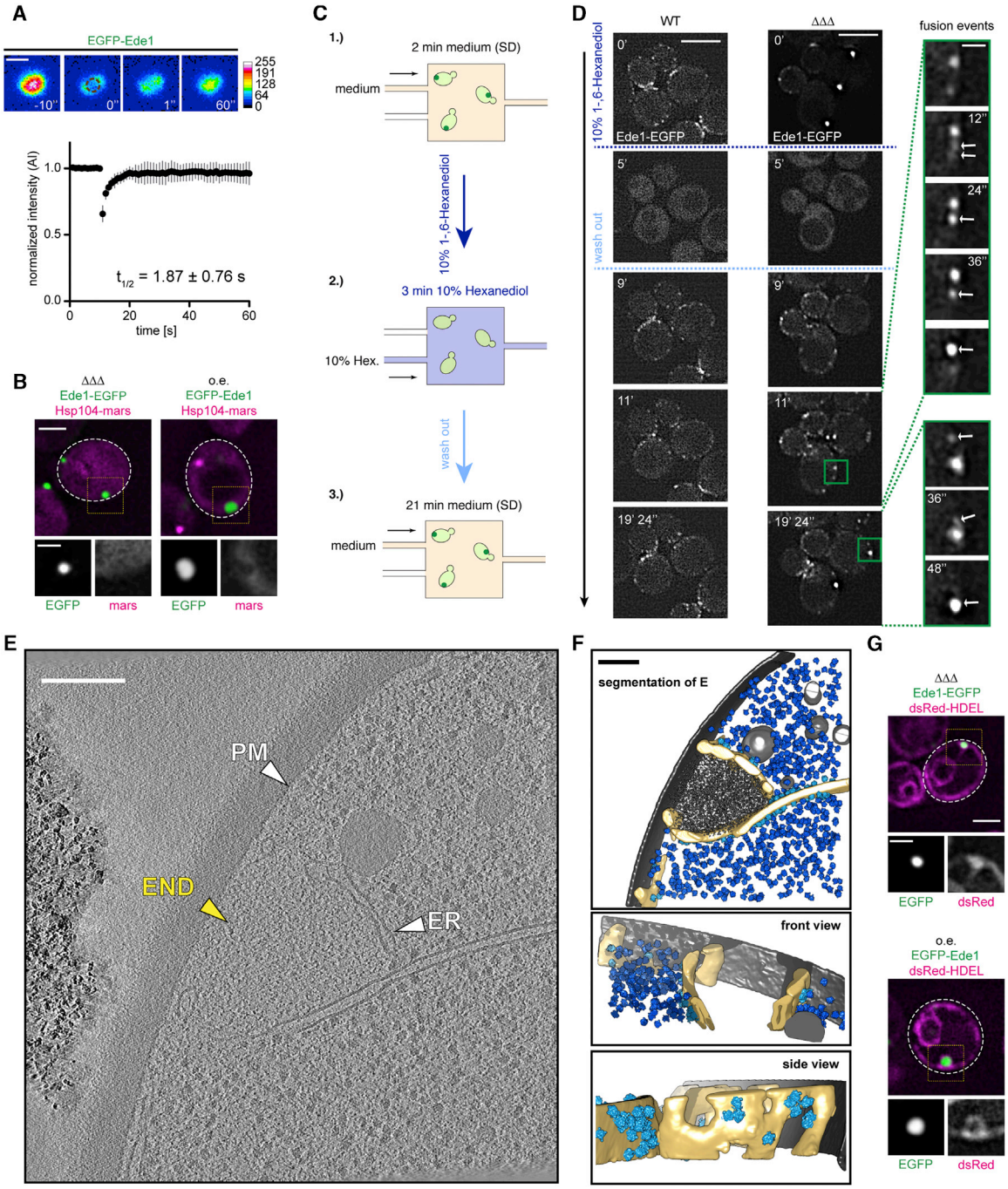

Figure 5. END Displays Hallmarks of LLPS

(A) FRAP experiments of EGFP-Ede1 (p*ADH*) clusters. A fraction within END was bleached (brown circle), and recovery of the signal was followed over a time course of 60 s (1 frame/1 s). Quantification shows the recovery of the EGFP-Ede1 signal from 13 independent experiments as mean ± SD. Scale bar, 1 μm.

(B) Colocalization experiments between Hsp104-mars and EGFP-Ede1 in ΔΔΔ cells (left) or between Hsp104-mars and EGFP-Ede1 (p*ADH*) (right). Scale bar, 2 μm; inset, 1 μm.

(C and D) Experimental setup to visualize the material properties of END in single cells. Tracking of the EGFP-Ede1 signal in WT and ΔΔΔ cells in a microfluidic device before, during, and after hexanediol treatment (C). After 2 min, the medium stream is switched to a medium containing 10% 1-,6-hexanediol and 10 μg/mL of digitonin for 3 min. Fluorescence images are recorded for 21 min (1 frame/12 s) after the medium was switched back (D). Scale bar, 5 μm; inset, 1 μm.

(E) Correlative cryo-ET of EGFP-Ede1 signal reveals architecture of END in ΔΔΔ cells. An average 2D section of the original tomogram shows a region correlated with the EGFP-Ede1 signal (marked in yellow). Scale bar, 200 nm.

(F) Top: segmentation of (E) shows the drop-like protein condensate (dark gray) at the PM, which is surrounded by a fenestrated membrane compartment (light yellow). Ribosomes are shown in light blue (membrane associated) and dark blue (free); PM is in dark gray. Middle: sliced-through front view of (E) without the

(legend continued on next page)

fluorescence of endogenously expressed EGFP-Ede1 in both WT and ΔΔΔ mutant cells before, during, and after hexanediol treatment (Figure 5C). A 3-min perfusion with hexanediol dissolved endocytic assemblies in both strains and led to dispersed cytosolic localization of Ede1. Following washout, EGFP-Ede1 started to re-accumulate at the PM. WT cells formed regular endocytic patches (Figure 5D; Video S1), whereas ΔΔΔ mutant cells additionally showed that individual endocytic patches fused into larger assemblies (Figure 5D; Video S2). Collectively, these data suggest that END is a dynamic compartment containing an ensemble of endocytic proteins exhibiting hallmarks of LLPS. This conclusion is corroborated by a study posted on bioRxiv during the course of our manuscript preparation (Kozak and Kaksonen, 2019).

Visualizing END Assemblies at the PM by Cryo-ET

To learn about their structural makeup, we applied high-resolution correlative cryo-electron tomography (cryo-ET) to END. To enrich for and localize those sites for structural studies *in situ*, we employed the ΔΔΔ strain, in which Ede1 was endogenously tagged with EGFP. This enabled targeted cryo-ET at sites of a correlated fluorescence signal on ~100-nm-thick lamellas obtained by 3D-correlative cryo-focused ion beam (cryo-FIB) milling (Figure S6C). Cryo-ET revealed several structural properties of those sites: (1) a distinct assembly with a drop-like shape, which localized proximal to the PM (Figures 5E, 5F, S6C, and S6D; Video S3); (2) no overtly regular or recognizable electron density in the droplet; (3) striking exclusion of ribosomes from the area attributed to END, emblematic of distinct assembles or organelles that are either tightly packed or have a specific boundary resembling exclusion zones observed during normal CME, although the area of condensation defining END was larger than regular exclusion zones (Kukulski et al., 2012; Takagi et al., 2003); and (4) a protein condensate surrounded by tubular membranes, which we attribute to ER based on associated ribosomes, as well as fluorescence imaging of the luminal ER marker dsRed-HDEL (Figures 5E–5G). Intriguingly, ER was not closed around END but formed a mesh with openings large enough for ribosomes to pass through (Figure 5F). This supports the notion that exclusion must occur by means other than membranes. The same characteristic features were observed for the strain in which EGFP-Ede1 was overexpressed (Figures S6D and S6E; Videos S4 and S5). The only notable difference was the increased volume occupied by the protein condensate compared with the ΔΔΔ strain, likely because of increased Ede1 levels.

Oligomerization and Condensation of Ede1 Are Important for Autophagic Degradation

To elucidate the molecular basis for END formation, we sought to identify domains in Ede1 responsible for LLPS. The well-characterized receptor p62 forms filaments that phase separate in the presence of ubiquitin chains to induce autophagy (Jakobi et al., 2020; Sun et al., 2018; Turco et al., 2019; Zaffagnini et al., 2018). To test roles of ubiquitin binding domains in CME constituents, we created a strain in which EGFP-Ede1 was overexpressed and the ubiquitin binding domains of Ede1, Ent1, and Ent2 were removed or mutated (*UBD*Δ) (Figure S7A). Although the average size of END was smaller, phase separation was not obviously impaired (Figure S7B). Accordingly, Ede1 binding to Atg8 was not impaired in the *UBD*Δ background, whereas binding of polyubiquitinated proteins was reduced (Figure S7C). Furthermore, EGFP′ still accumulated in the vacuole upon subjecting *UBD*Δ cells to nitrogen starvation (Figure S7D).

Because no evidence for ubiquitin-mediated phase separation was observed, we considered whether Ede1's multidomain structure may encompass a distinct element for phase separation. Many proteins undergoing LLPS contain intrinsically disordered low-complexity regions (LCRs), which are often necessary for driving intracellular phase transitions (Martin and Mittag, 2018). *In silico* analysis of the Ede1 sequence identified an LCR between the N-terminal EH domains and the central CC region overlapping the previously annotated proline-rich region (Figure 6A). Stepwise deletion from the N terminus showed that removal of LCR, but not of the EH domains alone, diminished Ede1 condensation. When most of the LCR was deleted (Ede1$^{549–1,381}$), Ede1 and END constituents Chc1 and Sla2 lost the ability to phase separate and became cytosolic (Figures 6A and 6B). In contrast, fusion of LCR alone to EGFP did not induce END formation (Figure 6C). LLPS was only observed for a EGFP fusion of LCR with CC, suggesting that CC-mediated oligomerization (Boeke et al., 2014) is a second requirement for END formation. In agreement with this concept, deletion of either LCR or CC alone diminished END formation (Figure S7E).

With mutant forms of Ede1 defective in phase separation, we could test its impact on autophagic degradation. The different N-terminal Ede1 deletion constructs were analyzed for autophagic turnover by GFP-cleavage assays, and autophagic degradation of Ede1 was correlated with its capacity to form condensates. The cytosolic Ede1$^{549–1,381}$ mutant was no longer degraded in the vacuole, and degradation of Ede1$^{525–1,381}$, which showed only slight condensation, was substantially inhibited (Figure 6D). Similar results were obtained when deleting just LCR or CC alone (Figure S7F). In addition, degradation of END constituents (Chc1 or Sla2) depended on Ede1 condensation (Figures 6E and S7G). For all Ede1 mutants, binding to Atg8 was not affected and we even detected binding of Ede1$^{549–1,381}$ to Atg8 by BiFC *in vivo* (Figures S7H and S7I), suggesting that interaction is not affected but that avid interactions are necessary to efficiently degrade the cargo.

To better understand what causes the transition from regular CME to END condensation, we performed an unbiased synthetic interaction screen using cells overexpressing EGFP-Ede1 (Figure S7J). This identified a strong negative genetic interaction with the gene encoding Sla1 (Figures S7J and S7K). Because

density corresponding to the endocytic protein accumulation. Bottom: fenestrated membrane compartment with membrane-associated ribosomes. Scale bar, 200 nm.

(G) Colocalization experiments between dsRed-HDEL and EGFP-Ede1 in ΔΔΔ cells (top) or between dsRed-HDEL and EGFP-Ede1 (p*ADH*) (bottom). Scale bar, 2 μm; inset, 1 μm.

See also Figure S6.

CellPress
OPEN ACCESS

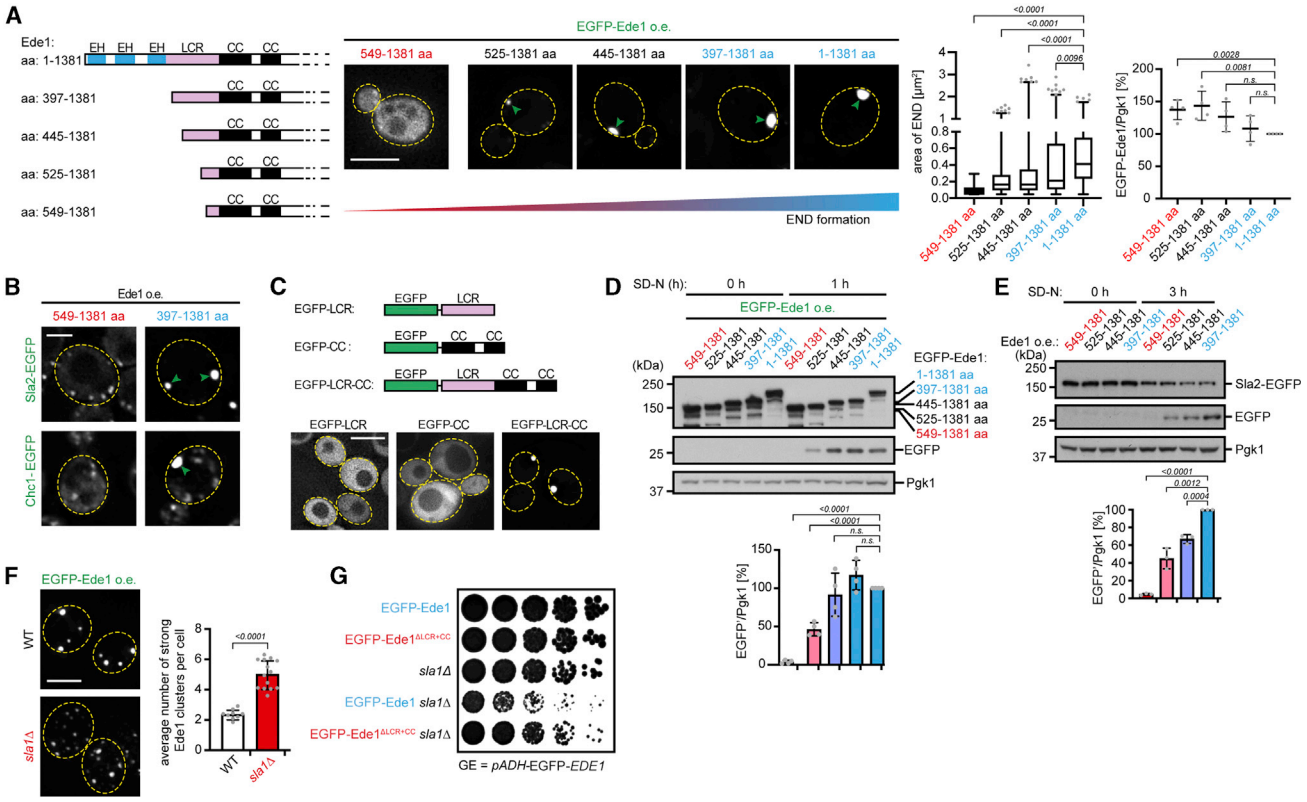

Figure 6. Phase Separation of Ede1 Is Essential for Autophagic END Degradation

(A) Monitoring of END formation in cells overexpressing different N-terminal truncations of EGFP-Ede1. Spot size was analyzed, computed from maximum z projections of the corresponding strains for more than 100 cells (n = 3 independent experiments). Protein levels were analyzed by WB and normalized against full-length Ede1 (n = 4). The illustration shows N-terminal truncation mutants used to map the region important for LLPS. Scale bar, 5 μm.

(B) Fluorescence microscopy of EGFP-tagged Sla2 or Chc1 in cells overexpressing Ede1$^{397–1,381}$ or Ede1$^{549–1,381}$ mutant (p*ADH*). Scale bar, 2 μm.

(C) Fluorescence images of cells expressing EGFP fusions of LCR, the CC domain, or both domains of Ede1; scale bar, 5 μm.

(D) Mutants overexpressing N-terminal EGFP-Ede1 truncations are analyzed by GFP-cleavage assay before and after 1 h of nitrogen starvation. Quantifications of EGFP′ levels normalized to Pgk1 are shown (n = 4).

(E) Cells coexpressing Sla2-EGFP and different N-terminal Ede1 truncation mutants (p*ADH*) are analyzed by GFP-cleavage assay before and after 3 h of nitrogen starvation. Quantifications are shown as in (D) (n = 3).

(F) END is monitored by overexpression of EGFP-Ede1 in WT and *sla1*Δ cells. Quantification shows the average number of ENDs per cell derived from WT cells (n = 9) and *sla1*Δ cells (n = 14). Maximum z projection is shown; scale bar, 5 μm.

(G) Spotting analysis of different mutant strains. Cells in log phase were spotted onto YPD plates and incubated for 3 days at 30°C.

For all quantifications, p values are calculated using two-tailed Student's t tests and data are mean ± SD. See also Figure S7.

Sla1 facilitates the transition of an endocytic patch from the early to the late phase (Carroll et al., 2012; Goode et al., 2015; Sun et al., 2015) and deletion of *SLA1* extends the early phase of endocytosis (Sun et al., 2017), we speculated that Ede1 overexpression in the *sla1*Δ mutant might globally affect endocytic assembly. Indeed, EGFP-Ede1 overexpression in *sla1*Δ cells led to an increase in the number of END assemblies (Figure 6F). To test whether the synthetic sickness depended on the ability of Ede1 to phase separate, we introduced Ede1$^{\Delta LCR+CC}$ into the *sla1*Δ background. In contrast to overexpression of WT Ede1 in *sla1*Δ mutant cells, Ede1$^{\Delta LCR+CC}$ did not show a synthetic growth phenotype, suggesting a crucial role for Ede1 phase separation (Figure 6G). Next, we tested whether autophagy can mitigate the toxic effect of Ede1 overexpression in *sla1*Δ. We controlled Ede1 expression by replacing the endogenous Ede1 promoter with a copper-inducible one. After lowering Ede1 expression by copper removal, followed by photometrically measuring of growth curves, we observed that *sla1*Δ cells that originally expressed WT Ede1 recovered faster than cells expressing Ede1^{AIMR} (Figure S7L). This rescue effect of WT Ede1 compared with Ede1^{AIMR} was even stronger when autophagy activity was upregulated by a 1.5 h pulse of nitrogen starvation before growth measurements, supporting the idea of a quality control function of the Ede1-dependent autophagy pathway.

Visualizing END Condensate Degradation

To examine the trajectory of END condensates from the PM to an autophagosome, we conducted fluorescence microscopy experiments using a microfluidic device and tracked EGFP-Ede1 and mCherry-Atg8 fluorescence in individual cells. After inducing nitrogen starvation to increase autophagic turnover, we observed clustering of mCherry-Atg8 specifically at sites of

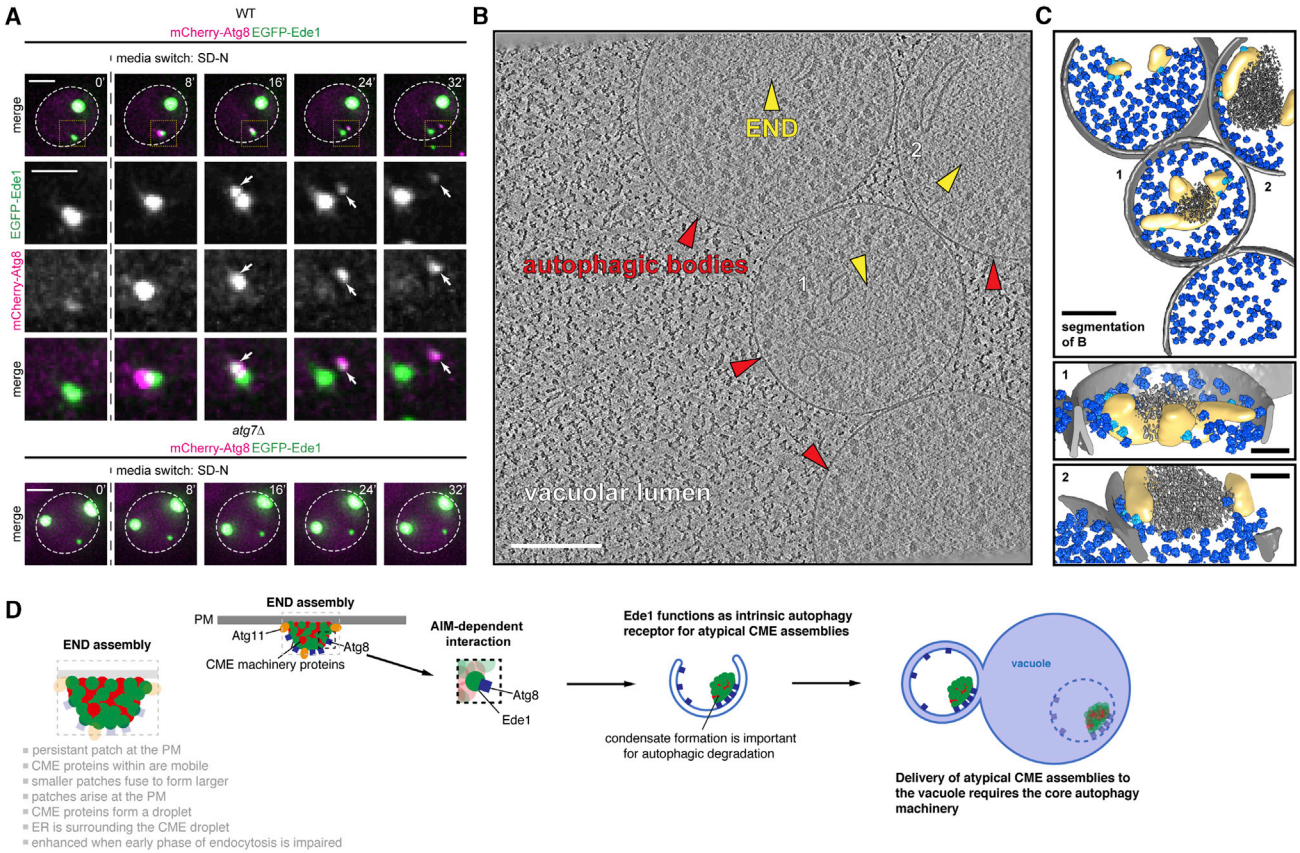

Figure 7. Visualization of Autophagic END Degradation

(A) Fluorescence microscopy of EGFP-Ede1 and mCherry-Atg8 (both p*ADH*) in WT or *atg7*Δ cells trapped in a microfluidic device after switching to synthetic minimal medium lacking nitrogen (SD-N) (8 min/1 frame). Maximum intensity z projections are shown for the individual time points. Scale bar, 2 μm; inset, 1 μm.

(B) Ultrastructural analysis of ΔΔΔ *atg15*Δ cells expressing EGFP-Ede1 by correlative cryo-ET after nitrogen starvation. The example shows EGFP-Ede1 accumulation, together with fenestrated ER, within autophagic bodies inside the vacuole. Shown is an average 2D section of the original tomogram. Scale bar, 200 nm.

(C) Segmentation of (B) shows END containing autophagic bodies. Color coding is the same as in Figure 5F. Insets show close-ups for END density corresponding to 1 and 2. Scale bar, 200 nm; inset, 100 nm.

(D) Overview of END and its Ede1-dependent autophagy pathway.

Ede1 accumulation. Small pieces pinched off of these structures into the cytosol in an Atg7-dependent manner and were positive for Atg8 and Ede1 (Figure 7A), suggesting that END is delivered in fractions to the vacuole.

To obtain snapshots of END condensates after delivery to autophagic bodies, we turned to cryo-ET in the ΔΔΔ *atg15*Δ strain. The fluorescent signal correlated with autophagic bodies within the lumen of the vacuole (Figure 7B). The structures inside these autophagic bodies were drop-like and similar to the ones observed earlier on the cytosolic side of the PM, despite being smaller. Ribosomes were likewise excluded from these condensates (Figure 7C; Video S6). Parts of the ER membrane were still attached to the CME condensates within the autophagic bodies (Figure 7C), suggesting a role of ER in preserving the condensate and/or in degradation. We also performed cryo-ET on cells grown in rich conditions to the early stationary phase. In contrast to the autophagic bodies seen under bulk conditions, these were smaller and exclusively contained END (Figure S7M; Video S7). Overall, the data visualize the presence of endocytic phase condensates within autophagic bodies.

DISCUSSION

In this study, we define a selective autophagy pathway, and its underlying mechanisms, from the point of cargo recognition to delivery to autophagosomes. We propose a model in which defects in the early phase of CME protein assembly trigger Ede1-mediated END formation (Figure 7D). Ede1 thereby plays a dual role as initiator of CME and as determinant for clearance of END assemblies via its built-in Atg8 recruitment signal. We propose calling such proteins intrinsic autophagy receptors, which are integral and functionally important subunits within normal complexes but can, if needed, direct them to autophagosomes for degradation. Consequently, intrinsic autophagy receptors may provide built-in quality control that differs from that of conventional receptors, which are dynamically recruited.

Intrinsic receptors are ideally positioned to distinguish normal from aberrant protein complexes. Other potential intrinsic receptors include the translocon subunit Sec62 and the nucleoporin Nup159 (Fumagalli et al., 2016; Lee et al., 2020a).

Central to the autophagic recognition of END assemblies is the ability of Ede1 to phase separate. Deletion of LCR and CC in Ede1, important for forming higher oligomeric cytosolic structures (Boeke et al., 2014), led to loss of its ability to undergo LLPS and abolished END formation. We suggest a model in which initially higher oligomeric structures are formed that phase separate and can form END. Given that cells contain numerous membraneless compartments, we anticipate that under different cellular conditions, there could be many other forms of selective autophagy, each with distinct cargo, awaiting discovery. The concept of intrinsic receptors might be expandable for other proteins driving LLPS.

Recently, it has been suggested that LLPS serves as a principal mechanism by which the complex assembly of CME proteins is achieved (Bergeron-Sandoval et al., 2018; Day et al., 2019; Kozak and Kaksonen, 2019). What restricts LLPS of CME proteins during regular endocytosis and inhibits END formation? LCR of Ede1 found to be indispensable for LLPS contains 20 experimentally validated phosphorylation sites. Introduction of negatively charged phosphoryl groups into Ede1 LCR would likely increase electrostatic repulsion between LCRs and might restrict self-assembly. Such a concept would be analogous to the LLPS protein FUS, in which phosphorylation in LCR disrupts phase separation (Monahan et al., 2017). Genetic perturbations of the early phase of endocytosis enhance formation of END assemblies. Although we do not know all functional consequences of these mutants, the major phenotype appears to be improper clathrin assembly (Boettner et al., 2011; Weinberg and Drubin, 2012). We speculate that CME proteins that are not involved in CME, because of subunit excess, defects, imperfect engagement with CME assemblies, or other defects, may provoke atypical assembly into phase-separated condensates with Ede1.

The condensation of END and its need for autophagic degradation suggests that highly avid interactions are necessary for efficient autophagic engulfment, which is in line with observations of other autophagy pathways (Zaffagnini and Martens, 2016). The ability of Ede1 to phase separate (Day et al., 2019) and to bind Atg8 is conserved in its mammalian and plant (*Arabidopsis*) orthologs (Bejarano et al., 2012; Wang et al., 2019), raising the possibility that the END autophagy pathway could be evolutionary conserved. Moreover, genetic perturbation of the early phase of endocytosis in human cells results in atypical accumulation of clathrin, Eps15, and AP2 at the PM (Kirchhausen et al., 2014; Mettlen et al., 2018; Meyerholz et al., 2005). Therefore, we anticipate that features regulating END condensates in *S. cerevisiae* most likely occur across species.

Finally, our ultrastructural dissection of END at the PM and within autophagic bodies provides insights of their cellular architecture. We observed the presence of fenestrated ER around END, which is intriguing, because ER is involved in autophagosome biogenesis (Hurley and Young, 2017; Mizushima et al., 2011; Noda and Inagaki, 2015; Shibutani and Yoshimori, 2014). However, parts of it appear to be degraded along with END. It is therefore appealing to speculate about a twofold involvement of ER—first, by providing a membrane source for autophagosome biogenesis (Maeda et al., 2019; Osawa et al., 2019; Schütter et al., 2020; Valverde et al., 2019) and, second, by regulating the dynamics of the END condensate, a concept recently proposed for processing bodies (Lee et al., 2020b). Future experiments are needed to determine the role of ER in this process. It seems likely that future studies will reveal other networks between membranes and phase-separated proteins in autophagy. A structural framework is now provided by visualization of such interactions spanning from the cytoplasm to autophagosomes.

STAR★METHODS

Detailed methods are provided in the online version of this paper and include the following:

- KEY RESOURCES TABLE
- RESOURCE AVAILABILITY
  - Lead Contact
  - Materials Availability
  - Data and Code Availability
- EXPERIMENTAL MODEL AND SUBJECT DETAILS
  - Yeast Cell Culture, Starvation, GFP Cleavage Assay, Spotting Assay and Cloning
- METHOD DETAILS
  - Immunoblot Techniques
  - Co-immunoprecipitation
  - Mass Spectrometry and Data Analysis
  - Protein Sample Production for Crystallography
  - Crystallization of Ede1-Atg8 Complex
  - Data Collection, Processing, Refinement and Deposition
  - Expression and Purification of GST-fusion Proteins and His-Atg8
  - Atg8 *In Vitro* Binding Assay
  - GST-Atg8 Pulldown with Yeast Cell Extract
  - Fluorescence Microscopy
  - FRAP and FLIP Analysis
  - Yeast Spot Analysis
  - Microfluidics Experiments
  - Automated Yeast Library Manipulations and High-throughput Microscopy
  - Electron Microscopy
  - Visualization
  - Isothermal Titration Calorimetry (ITC)
- QUANTIFICATION AND STATISTICAL ANALYSIS

SUPPLEMENTAL INFORMATION

Supplemental Information can be found online at https://doi.org/10.1016/j.molcel.2020.10.030.

ACKNOWLEDGMENTS

We thank S. Schkoelziger, S. Kienle, and L. Rieger for technical assistance and J. Rech for help with robot-based techniques; the MPIB Imaging and Biochemistry Core Facility for help with image analysis (G. Cardone and M. Spitaler) and mass spectrometry analysis (N. Nagaraj and S. Uebel); D. Scott

and S. Jayaraman for help with crystallography; T. Wollert and S. Emr for reagents; J. Plitzko and M. Schaffer for microscope support; U. Hartl and M. Hayer-Hartl for discussions; and A. Bieber and C. Capitanio for critical reading of the manuscript. This work was supported by the Max Planck Society (to S.J., B.P., B.A.S., and W.B.), the Deutsche Forschungsgemeinschaft (DFG, German Research Foundation) (to S.J., B.P., B.A.S. [SCHU 3196/1-1], and W.B.), the Center for Integrated Protein Science Munich (to S.J.), an ERC advanced grant (ERC-2013-AdG-339176 to S.J.), the Louis-Jeantet Foundation (to S.J.), NIH R37GM069530, St. Jude Children's Research Hospital, and ALSAC (to B.A.S. and Y.Z.). F.W. was supported by an EMBO long-term fellowship (ALTF 764-2014). P.S.E. was supported by an Alexander von Humboldt returners fellowship. Data were collected at SER-CAT 22-BM at the APS Argonne National Lab, supported in part by NIHS10_RR25528 and S10_RR028976.

AUTHORS CONTRIBUTIONS

Conceptualization, S.J. and F.W.; Methodology, F.W., P.S.E., S.J., B.P., B.A.S., and W.B.; Investigation, F.W., C.-W.L., Y.Z., D.S., and P.S.E.; Writing – Original Draft, F.W.; Writing – Review & Editing, F.W., B.P., P.S.E., B.A.S., and W.B.; Supervision, B.P., B.A.S., and W.B.; Funding Acquisition, S.J., B.A.S., and W.B.; Resources, S.J., B.A.S., and W.B.

DECLARATION OF INTERESTS

The authors declare no competing interests.

Received: May 15, 2020
Revised: September 20, 2020
Accepted: October 21, 2020
Published: November 17, 2020

REFERENCES

Alberti, S., Gladfelter, A., and Mittag, T. (2019). Considerations and Challenges in Studying Liquid-Liquid Phase Separation and Biomolecular Condensates. Cell *176*, 419–434.

Arnold, J., Mahamid, J., Lucic, V., de Marco, A., Fernandez, J.J., Laugks, T., Mayer, T., Hyman, A.A., Baumeister, W., and Plitzko, J.M. (2016). Site-Specific Cryo-focused Ion Beam Sample Preparation Guided by 3D Correlative Microscopy. Biophys. J. *110*, 860–869.

Ashburner, M., Ball, C.A., Blake, J.A., Botstein, D., Butler, H., Cherry, J.M., Davis, A.P., Dolinski, K., Dwight, S.S., Eppig, J.T., et al.; The Gene Ontology Consortium (2000). Gene ontology: tool for the unification of biology. Nat. Genet. *25*, 25–29.

Banani, S.F., Lee, H.O., Hyman, A.A., and Rosen, M.K. (2017). Biomolecular condensates: organizers of cellular biochemistry. Nat. Rev. Mol. Cell Biol. *18*, 285–298.

Behrends, C., Sowa, M.E., Gygi, S.P., and Harper, J.W. (2010). Network organization of the human autophagy system. Nature *466*, 68–76.

Bejarano, E., Girao, H., Yuste, A., Patel, B., Marques, C., Spray, D.C., Pereira, P., and Cuervo, A.M. (2012). Autophagy modulates dynamics of connexins at the plasma membrane in a ubiquitin-dependent manner. Mol. Biol. Cell *23*, 2156–2169.

Bergeron-Sandoval, L.-P., Heris, H.K., Chang, C., Cornell, C.E., Keller, S.L., François, P., Hendricks, A.G., Ehrlicher, A.J., Pappu, R.V., and Michnick, S.W. (2018). Endocytosis caused by liquid-liquid phase separation of proteins. bioRxiv. https://doi.org/10.1101/145664.

Boeke, D., Trautmann, S., Meurer, M., Wachsmuth, M., Godlee, C., Knop, M., and Kaksonen, M. (2014). Quantification of cytosolic interactions identifies Ede1 oligomers as key organizers of endocytosis. Mol. Syst. Biol. *10*, 756.

Boettner, D.R., Chi, R.J., and Lemmon, S.K. (2011). Lessons from yeast for clathrin-mediated endocytosis. Nat. Cell Biol. *14*, 2–10.

Burnley, T., Palmer, C.M., and Winn, M. (2017). Recent developments in the CCP-EM software suite. Acta Crystallogr. D Struct. Biol. *73*, 469–477.

Carpenter, A.E., Jones, T.R., Lamprecht, M.R., Clarke, C., Kang, I.H., Friman, O., Guertin, D.A., Chang, J.H., Lindquist, R.A., Moffat, J., et al. (2006). CellProfiler: image analysis software for identifying and quantifying cell phenotypes. Genome Biol. *7*, R100.

Carroll, S.Y., Stimpson, H.E., Weinberg, J., Toret, C.P., Sun, Y., and Drubin, D.G. (2012). Analysis of yeast endocytic site formation and maturation through a regulatory transition point. Mol. Biol. Cell *23*, 657–668.

Cheong, H., and Klionsky, D.J. (2008). Biochemical methods to monitor autophagy-related processes in yeast. Methods Enzymol. *451*, 1–26.

Collins, S.R., Roguev, A., and Krogan, N.J. (2010). Quantitative genetic interaction mapping using the E-MAP approach. Methods Enzymol. *470*, 205–231.

Cox, J., and Mann, M. (2008). MaxQuant enables high peptide identification rates, individualized p.p.b.-range mass accuracies and proteome-wide protein quantification. Nat. Biotechnol. *26*, 1367–1372.

Cox, J., Hein, M.Y., Luber, C.A., Paron, I., Nagaraj, N., and Mann, M. (2014). Accurate proteome-wide label-free quantification by delayed normalization and maximal peptide ratio extraction, termed MaxLFQ. Mol. Cell. Proteomics *13*, 2513–2526.

Day, K.J., Kago, G., Wang, L., Richter, J.B., Hayden, C.C., Lafer, E.M., and Stachowiak, J.C. (2019). Liquid-like protein interactions catalyze assembly of endocytic vesicles. bioRxiv. https://doi.org/10.1101/860684.

Dikic, I. (2017). Proteasomal and Autophagic Degradation Systems. Annu. Rev. Biochem. *86*, 193–224.

Dikic, I., and Elazar, Z. (2018). Mechanism and medical implications of mammalian autophagy. Nat. Rev. Mol. Cell Biol. *19*, 349–364.

Dores, M.R., Schnell, J.D., Maldonado-Baez, L., Wendland, B., and Hicke, L. (2010). The function of yeast epsin and Ede1 ubiquitin-binding domains during receptor internalization. Traffic *11*, 151–160.

Dunham, M.J., Dunham, M.J., Gartenberg, M.R., and Brown, G.W. (2015). Methods in yeast genetics and genomics: a Cold Spring Harbor Laboratory course manual (Cold Spring Harbor Laboratory Press).

Emsley, P., and Cowtan, K. (2004). Coot: model-building tools for molecular graphics. Acta Crystallogr. D Biol. Crystallogr. *60*, 2126–2132.

Emsley, P., Lohkamp, B., Scott, W.G., and Cowtan, K. (2010). Features and development of Coot. Acta Crystallogr. D Biol. Crystallogr. *66*, 486–501.

Epple, U.D., Suriapranata, I., Eskelinen, E.L., and Thumm, M. (2001). Aut5/Cvt17p, a putative lipase essential for disintegration of autophagic bodies inside the vacuole. J. Bacteriol. *183*, 5942–5955.

Farré, J.C., and Subramani, S. (2016). Mechanistic insights into selective autophagy pathways: lessons from yeast. Nat. Rev. Mol. Cell Biol. *17*, 537–552.

Fumagalli, F., Noack, J., Bergmann, T.J., Cebollero, E., Pisoni, G.B., Fasana, E., Fregno, I., Galli, C., Loi, M., Soldà, T., et al. (2016). Translocon component Sec62 acts in endoplasmic reticulum turnover during stress recovery. Nat. Cell Biol. *18*, 1173–1184.

Gatica, D., Lahiri, V., and Klionsky, D.J. (2018). Cargo recognition and degradation by selective autophagy. Nat. Cell Biol. *20*, 233–242.

Goode, B.L., Eskin, J.A., and Wendland, B. (2015). Actin and endocytosis in budding yeast. Genetics *199*, 315–358.

Hagen, W.J.H., Wan, W., and Briggs, J.A.G. (2017). Implementation of a cryo-electron tomography tilt-scheme optimized for high resolution subtomogram averaging. J. Struct. Biol. *197*, 191–198.

Harmon, T.S., Holehouse, A.S., Rosen, M.K., and Pappu, R.V. (2017). Intrinsically disordered linkers determine the interplay between phase separation and gelation in multivalent proteins. eLife *6*, e30294.

Ho, K.H., Chang, H.E., and Huang, W.P. (2009). Mutation at the cargo-receptor binding site of Atg8 also affects its general autophagy regulation function. Autophagy *5*, 461–471.

Hrabe, T., Chen, Y., Pfeffer, S., Cuellar, L.K., Mangold, A.V., and Förster, F. (2012). PyTom: a python-based toolbox for localization of macromolecules in cryo-electron tomograms and subtomogram analysis. J. Struct. Biol. *178*, 177–188.

Hubner, N.C., Bird, A.W., Cox, J., Splettstoesser, B., Bandilla, P., Poser, I., Hyman, A., and Mann, M. (2010). Quantitative proteomics combined with BAC TransgeneOmics reveals *in vivo* protein interactions. J. Cell Biol. *189*, 739–754.

Hurley, J.H., and Young, L.N. (2017). Mechanisms of Autophagy Initiation. Annu. Rev. Biochem. *86*, 225–244.

Inoue, Y., Taguchi, H., Kishimoto, A., and Yoshida, M. (2004). Hsp104 binds to yeast Sup35 prion fiber but needs other factor(s) to sever it. J. Biol. Chem. *279*, 52319–52323.

Jakobi, A.J., Huber, S.T., Mortensen, S.A., Schultz, S.W., Palara, A., Kuhm, T., Shrestha, B.K., Lamark, T., Hagen, W.J.H., Wilmanns, M., et al. (2020). Structural basis of p62/SQSTM1 helical filaments and their role in cellular cargo uptake. Nat. Commun. *11*, 440.

Johansen, T., and Lamark, T. (2020). Selective Autophagy: ATG8 Family Proteins, LIR Motifs and Cargo Receptors. J. Mol. Biol. *432*, 80–103.

Jones, T.R., Kang, I.H., Wheeler, D.B., Lindquist, R.A., Papallo, A., Sabatini, D.M., Golland, P., and Carpenter, A.E. (2008). CellProfiler Analyst: data exploration and analysis software for complex image-based screens. BMC Bioinformatics *9*, 482.

Kalvari, I., Tsompanis, S., Mulakkal, N.C., Osgood, R., Johansen, T., Nezis, I.P., and Promponas, V.J. (2014). iLIR: A web resource for prediction of Atg8-family interacting proteins. Autophagy *10*, 913–925.

Kamber, R.A., Shoemaker, C.J., and Denic, V. (2015). Receptor-Bound Targets of Selective Autophagy Use a Scaffold Protein to Activate the Atg1 Kinase. Mol. Cell *59*, 372–381.

Kim, J., Kamada, Y., Stromhaug, P.E., Guan, J., Hefner-Gravink, A., Baba, M., Scott, S.V., Ohsumi, Y., Dunn, W.A., Jr., and Klionsky, D.J. (2001). Cvt9/Gsa9 functions in sequestering selective cytosolic cargo destined for the vacuole. J. Cell Biol. *153*, 381–396.

Kirchhausen, T., Owen, D., and Harrison, S.C. (2014). Molecular structure, function, and dynamics of clathrin-mediated membrane traffic. Cold Spring Harb. Perspect. Biol. *6*, a016725.

Kirkin, V., and Rogov, V.V. (2019). A Diversity of Selective Autophagy Receptors Determines the Specificity of the Autophagy Pathway. Mol. Cell *76*, 268–285.

Kirmitzoglou, I., and Promponas, V.J. (2015). LCR-eXXXplorer: a web platform to search, visualize and share data for low complexity regions in protein sequences. Bioinformatics *31*, 2208–2210.

Knop, M., Siegers, K., Pereira, G., Zachariae, W., Winsor, B., Nasmyth, K., and Schiebel, E. (1999). Epitope tagging of yeast genes using a PCR-based strategy: more tags and improved practical routines. Yeast *15* (10B), 963–972.

Kozak, M., and Kaksonen, M. (2019). Phase separation of Ede1 promotes the initiation of endocytic events. bioRxiv. https://doi.org/10.1101/861203.

Kremer, J.R., Mastronarde, D.N., and McIntosh, J.R. (1996). Computer visualization of three-dimensional image data using IMOD. J. Struct. Biol. *116*, 71–76.

Kukulski, W., Schorb, M., Kaksonen, M., and Briggs, J.A. (2012). Plasma membrane reshaping during endocytosis is revealed by time-resolved electron tomography. Cell *150*, 508–520.

Lee, C.W., Wilfling, F., Ronchi, P., Allegretti, M., Mosalaganti, S., Jentsch, S., Beck, M., and Pfander, B. (2020a). Selective autophagy degrades nuclear pore complexes. Nat. Cell Biol. *22*, 159–166.

Lee, J.E., Cathey, P.I., Wu, H., Parker, R., and Voeltz, G.K. (2020b). Endoplasmic reticulum contact sites regulate the dynamics of membraneless organelles. Science *367*, eaay7108.

Li, J., Zhu, R., Chen, K., Zheng, H., Zhao, H., Yuan, C., Zhang, H., Wang, C., and Zhang, M. (2018). Potent and specific Atg8-targeting autophagy inhibitory peptides from giant ankyrins. Nat. Chem. Biol. *14*, 778–787.

Liebschner, D., Afonine, P.V., Baker, M.L., Bunkóczi, G., Chen, V.B., Croll, T.I., Hintze, B., Hung, L.W., Jain, S., McCoy, A.J., et al. (2019). Macromolecular structure determination using X-rays, neutrons and electrons: recent developments in Phenix. Acta Crystallogr. D Struct. Biol. *75*, 861–877.

Lu, K., Psakhye, I., and Jentsch, S. (2014). Autophagic clearance of polyQ proteins mediated by ubiquitin-Atg8 adaptors of the conserved CUET protein family. Cell *158*, 549–563.

Lu, R., Drubin, D.G., and Sun, Y. (2016). Clathrin-mediated endocytosis in budding yeast at a glance. J. Cell Sci. *129*, 1531–1536.

Lu, A.X., Zarin, T., Hsu, I.S., and Moses, A.M. (2019). YeastSpotter: accurate and parameter-free web segmentation for microscopy images of yeast cells. Bioinformatics *35*, 4525–4527.

Maeda, S., Otomo, C., and Otomo, T. (2019). The autophagic membrane tether ATG2A transfers lipids between membranes. eLife *8*, e45777.

Martin, E.W., and Mittag, T. (2018). Relationship of Sequence and Phase Separation in Protein Low-Complexity Regions. Biochemistry *57*, 2478–2487.

Mastronarde, D.N. (2005). Automated electron microscope tomography using robust prediction of specimen movements. J. Struct. Biol. *152*, 36–51.

Matscheko, N., Mayrhofer, P., Rao, Y., Beier, V., and Wollert, T. (2019). Atg11 tethers Atg9 vesicles to initiate selective autophagy. PLoS Biol. *17*, e3000377.

Merrifield, C.J., and Kaksonen, M. (2014). Endocytic accessory factors and regulation of clathrin-mediated endocytosis. Cold Spring Harb. Perspect. Biol. *6*, a016733.

Mettlen, M., Chen, P.H., Srinivasan, S., Danuser, G., and Schmid, S.L. (2018). Regulation of Clathrin-Mediated Endocytosis. Annu. Rev. Biochem. *87*, 871–896.

Meyerholz, A., Hinrichsen, L., Groos, S., Esk, P.C., Brandes, G., and Ungewickell, E.J. (2005). Effect of clathrin assembly lymphoid myeloid leukemia protein depletion on clathrin coat formation. Traffic *6*, 1225–1234.

Mizushima, N., Yoshimori, T., and Ohsumi, Y. (2011). The role of Atg proteins in autophagosome formation. Annu. Rev. Cell Dev. Biol. *27*, 107–132.

Mochida, K., Oikawa, Y., Kimura, Y., Kirisako, H., Hirano, H., Ohsumi, Y., and Nakatogawa, H. (2015). Receptor-mediated selective autophagy degrades the endoplasmic reticulum and the nucleus. Nature *522*, 359–362.

Monahan, Z., Ryan, V.H., Janke, A.M., Burke, K.A., Rhoads, S.N., Zerze, G.H., O'Meally, R., Dignon, G.L., Conicella, A.E., Zheng, W., et al. (2017). Phosphorylation of the FUS low-complexity domain disrupts phase separation, aggregation, and toxicity. EMBO J. *36*, 2951–2967.

Nakatogawa, H., Suzuki, K., Kamada, Y., and Ohsumi, Y. (2009). Dynamics and diversity in autophagy mechanisms: lessons from yeast. Nat. Rev. Mol. Cell Biol. *10*, 458–467.

Noda, N.N., and Inagaki, F. (2015). Mechanisms of Autophagy. Annu. Rev. Biophys. *44*, 101–122.

Noda, T., and Ohsumi, Y. (1998). Tor, a phosphatidylinositol kinase homologue, controls autophagy in yeast. J. Biol. Chem. *273*, 3963–3966.

Noda, N.N., Ohsumi, Y., and Inagaki, F. (2010). Atg8-family interacting motif crucial for selective autophagy. FEBS Lett. *584*, 1379–1385.

Ohsumi, Y. (2001). Molecular dissection of autophagy: two ubiquitin-like systems. Nat. Rev. Mol. Cell Biol. *2*, 211–216.

Osawa, T., Kotani, T., Kawaoka, T., Hirata, E., Suzuki, K., Nakatogawa, H., Ohsumi, Y., and Noda, N.N. (2019). Atg2 mediates direct lipid transfer between membranes for autophagosome formation. Nat. Struct. Mol. Biol. *26*, 281–288.

Otwinowski, Z., and Minor, W. (1997). Processing of X-ray diffraction data collected in oscillation mode. Methods Enzymol. *276*, 307–326.

Perez-Riverol, Y., Csordas, A., Bai, J., Bernal-Llinares, M., Hewapathirana, S., Kundu, D.J., Inuganti, A., Griss, J., Mayer, G., Eisenacher, M., et al. (2019). The PRIDE database and related tools and resources in 2019: improving support for quantification data. Nucleic Acids Res. *47* (D1), D442–D450.

Pettersen, E.F., Goddard, T.D., Huang, C.C., Couch, G.S., Greenblatt, D.M., Meng, E.C., and Ferrin, T.E. (2004). UCSF Chimera—a visualization system for exploratory research and analysis. J. Comput. Chem. *25*, 1605–1612.

Phair, R.D., Gorski, S.A., and Misteli, T. (2004). Measurement of dynamic protein binding to chromatin *in vivo*, using photobleaching microscopy. Methods Enzymol. *375*, 393–414.

Popelka, H., and Klionsky, D.J. (2015). Analysis of the native conformation of the LIR/AIM motif in the Atg8/LC3/GABARAP-binding proteins. Autophagy *11*, 2153–2159.

Rappsilber, J., Ishihama, Y., and Mann, M. (2003). Stop and go extraction tips for matrix-assisted laser desorption/ionization, nanoelectrospray, and LC/MS sample pretreatment in proteomics. Anal. Chem. *75*, 663–670.

Reggiori, F., Komatsu, M., Finley, K., and Simonsen, A. (2012). Autophagy: more than a nonselective pathway. Int. J. Cell Biol. *2012*, 219625.

Rigort, A., Bäuerlein, F.J., Leis, A., Gruska, M., Hoffmann, C., Laugks, T., Böhm, U., Eibauer, M., Gnaegi, H., Baumeister, W., and Plitzko, J.M. (2010). Micromachining tools and correlative approaches for cellular cryo-electron tomography. J. Struct. Biol. *172*, 169–179.

Rohou, A., and Grigorieff, N. (2015). CTFFIND4: Fast and accurate defocus estimation from electron micrographs. J. Struct. Biol. *192*, 216–221.

Schaffer, M., Mahamid, J., Engel, B.D., Laugks, T., Baumeister, W., and Plitzko, J.M. (2017). Optimized cryo-focused ion beam sample preparation aimed at *in situ* structural studies of membrane proteins. J. Struct. Biol. *197*, 73–82.

Scheres, S.H. (2012). RELION: implementation of a Bayesian approach to cryo-EM structure determination. J. Struct. Biol. *180*, 519–530.

Schindelin, J., Arganda-Carreras, I., Frise, E., Kaynig, V., Longair, M., Pietzsch, T., Preibisch, S., Rueden, C., Saalfeld, S., Schmid, B., et al. (2012). Fiji: an open-source platform for biological-image analysis. Nat. Methods *9*, 676–682.

Schneider, C.A., Rasband, W.S., and Eliceiri, K.W. (2012). NIH Image to ImageJ: 25 years of image analysis. Nat. Methods *9*, 671–675.

Schütter, M., Giavalisco, P., Brodesser, S., and Graef, M. (2020). Local Fatty Acid Channeling into Phospholipid Synthesis Drives Phagophore Expansion during Autophagy. Cell *180*, 135–149.

Sherman, F. (2002). Getting started with yeast. Methods Enzymol. *350*, 3–41.

Shibutani, S.T., and Yoshimori, T. (2014). A current perspective of autophagosome biogenesis. Cell Res. *24*, 58–68.

Shintani, T., and Klionsky, D.J. (2004). Cargo proteins facilitate the formation of transport vesicles in the cytoplasm to vacuole targeting pathway. J. Biol. Chem. *279*, 29889–29894.

Shorter, J., and Lindquist, S. (2004). Hsp104 catalyzes formation and elimination of self-replicating Sup35 prion conformers. Science *304*, 1793–1797.

Smith, S.M., Baker, M., Halebian, M., and Smith, C.J. (2017). Weak Molecular Interactions in Clathrin-Mediated Endocytosis. Front. Mol. Biosci. *4*, 72.

Snapp, E.L. (2013). Photobleaching methods to study Golgi complex dynamics in living cells. Methods Cell Biol. *118*, 195–216.

Sun, Y., Leong, N.T., Wong, T., and Drubin, D.G. (2015). A Pan1/End3/Sla1 complex links Arp2/3-mediated actin assembly to sites of clathrin-mediated endocytosis. Mol. Biol. Cell *26*, 3841–3856.

Sun, Y., Leong, N.T., Jiang, T., Tangara, A., Darzacq, X., and Drubin, D.G. (2017). Switch-like Arp2/3 activation upon WASP and WIP recruitment to an apparent threshold level by multivalent linker proteins *in vivo*. eLife *6*, e29140.

Sun, D., Wu, R., Zheng, J., Li, P., and Yu, L. (2018). Polyubiquitin chain-induced p62 phase separation drives autophagic cargo segregation. Cell Res. *28*, 405–415.

Szklarczyk, D., Gable, A.L., Lyon, D., Junge, A., Wyder, S., Huerta-Cepas, J., Simonovic, M., Doncheva, N.T., Morris, J.H., Bork, P., et al. (2019). STRING v11: protein-protein association networks with increased coverage, supporting functional discovery in genome-wide experimental datasets. Nucleic Acids Res. *47* (D1), D607–D613.

Takagi, T., Ishijima, S.A., Ochi, H., and Osumi, M. (2003). Ultrastructure and behavior of actin cytoskeleton during cell wall formation in the fission yeast *Schizosaccharomyces pombe*. J. Electron Microsc. (Tokyo) *52*, 161–174.

Tal, R., Winter, G., Ecker, N., Klionsky, D.J., and Abeliovich, H. (2007). Aup1p, a yeast mitochondrial protein phosphatase homolog, is required for efficient stationary phase mitophagy and cell survival. J. Biol. Chem. *282*, 5617–5624.

Tong, A.H., and Boone, C. (2006). Synthetic genetic array analysis in *Saccharomyces cerevisiae*. Methods Mol. Biol. *313*, 171–192.

Torggler, R., Papinski, D., Brach, T., Bas, L., Schuschnig, M., Pfaffenwimmer, T., Rohringer, S., Matzhold, T., Schweida, D., Brezovich, A., and Kraft, C. (2016). Two Independent Pathways within Selective Autophagy Converge to Activate Atg1 Kinase at the Vacuole. Mol. Cell *64*, 221–235.

Turco, E., Witt, M., Abert, C., Bock-Bierbaum, T., Su, M.Y., Trapannone, R., Sztacho, M., Danieli, A., Shi, X., Zaffagnini, G., et al. (2019). FIP200 Claw Domain Binding to p62 Promotes Autophagosome Formation at Ubiquitin Condensates. Mol. Cell *74*, 330–346.

Tyanova, S., Temu, T., Sinitcyn, P., Carlson, A., Hein, M.Y., Geiger, T., Mann, M., and Cox, J. (2016). The Perseus computational platform for comprehensive analysis of (prote)omics data. Nat. Methods *13*, 731–740.

Ulrich, H.D., and Jentsch, S. (2000). Two RING finger proteins mediate cooperation between ubiquitin-conjugating enzymes in DNA repair. EMBO J. *19*, 3388–3397.

Valverde, D.P., Yu, S., Boggavarapu, V., Kumar, N., Lees, J.A., Walz, T., Reinisch, K.M., and Melia, T.J. (2019). ATG2 transports lipids to promote autophagosome biogenesis. J. Cell Biol. *218*, 1787–1798.

Wang, P., Pleskot, R., Zang, J., Winkler, J., Wang, J., Yperman, K., Zhang, T., Wang, K., Gong, J., Guan, Y., et al. (2019). Plant AtEH/Pan1 proteins drive autophagosome formation at ER-PM contact sites with actin and endocytic machinery. Nat. Commun. *10*, 5132.

Weinberg, J., and Drubin, D.G. (2012). Clathrin-mediated endocytosis in budding yeast. Trends Cell Biol. *22*, 1–13.

Wen, X., and Klionsky, D.J. (2016). An overview of macroautophagy in yeast. J. Mol. Biol. *428* (9 Pt A), 1681–1699.

Yamasaki, A., Alam, J.M., Noshiro, D., Hirata, E., Fujioka, Y., Suzuki, K., Ohsumi, Y., and Noda, N.N. (2020). Liquidity Is a Critical Determinant for Selective Autophagy of Protein Condensates. Mol. Cell *77*, 1163–1175.

Yorimitsu, T., and Klionsky, D.J. (2005). Atg11 links cargo to the vesicle-forming machinery in the cytoplasm to vacuole targeting pathway. Mol. Biol. Cell *16*, 1593–1605.

Zaffagnini, G., and Martens, S. (2016). Mechanisms of Selective Autophagy. J. Mol. Biol. *428* (9 Pt A), 1714–1724.

Zaffagnini, G., Savova, A., Danieli, A., Romanov, J., Tremel, S., Ebner, M., Peterbauer, T., Sztacho, M., Trapannone, R., Tarafder, A.K., et al. (2018). p62 filaments capture and present ubiquitinated cargos for autophagy. EMBO J. *37*, e98308.

Zheng, S.Q., Palovcak, E., Armache, J.P., Verba, K.A., Cheng, Y., and Agard, D.A. (2017a). MotionCor2: anisotropic correction of beam-induced motion for improved cryo-electron microscopy. Nat. Methods *14*, 331–332.

Zheng, Y., Qiu, Y., Gunderson, J.E., and Schulman, B.A. (2017b). Production of Human ATG Proteins for Lipidation Assays. Methods Enzymol. *587*, 97–113.

STAR★METHODS

KEY RESOURCES TABLE

REAGENT or RESOURCE	SOURCE	IDENTIFIER
Antibodies		
Mouse monoclonal anti-HA-tag (clone F-7)	Santa Cruz	Cat# sc-7392; RRID: AB_627809
Mouse monoclonal anti-Ubiquitin (clone P4D1)	Santa Cruz	Cat# sc-8017; RRID: AB_628423
Mouse monoclonal anti-GFP (clone B-2)	Santa Cruz	Cat# sc-9996; RRID: AB_627695
Mouse monoclonal anti-Pma1 (clone 40B7)	Invitrogen	Cat# MA1-91567; RRID: AB_1959827
Mouse monoclonal anti-Dpm1 (clone 5C5A7)	Invitrogen	Cat# A-6429; RRID: AB_2536204
Mouse monoclonal anti-Pgk1 (clone 22C5D8)	Invitrogen	Cat# 459250; RRID: AB_2532235
Mouse monoclonal anti-GFP (clones 7.1 and 13.1)	Sigma	Cat# 11814460001; RRID: AB_390913
Rabbit polyclonal anti-Ape1	Dr. Thomas Wollert	N/A
Rabbit polyclonal anti-Atg8	MPIB	N/A
Rabbit polyclonal anti-Ede1 (aa 1-400)	MPIB	N/A
Rabbit polyclonal peroxidase anti-peroxidase	Sigma	Cat# P1291; RRID: AB_1079562
Bacterial and Virus Strains		
E. coli Rosetta™ 2(DE3)	Novagen	Cat# 71400
E. coli Rosetta™ 2(DE3)pLysS	Novagen	Cat# 71403
Chemicals, Peptides, and Recombinant Proteins		
cOmplete EDTA-free protease inhibitor cocktail	Roche	Cat# 05056489001
PhosSTOP™ phosphatase inhibitor tablets	Roche	Cat# 4906837001
Pefabloc® SC	Roche	Cat# 11585916001
1,6-Hexanediol	Sigma	Cat# H11807-1KG
PMSF	Roche	Cat# 11359061001
N-Ethylmaleimide (NEM)	Sigma	Cat# E3876
BD Difco™ Yeast Nitrogen Base w/o Amino Acids and Ammonium Sulfates	Thermo Scientific	Cat# 11743014
Yeast Nitrogen Base w/o Amino Acids and w/o Folic Acid and Riboflavin. LOFLO	Formedium	Cat# CYN6501
Rapamycin	AbMole BioScience	Cat# M1768
PageBlue Protein Staining Solution	Thermo Scientific	Cat# 24620
Critical Commercial Assays		
GFP-Trap® Agarose	ChromoTek	Cat# gta-10
GFP-Trap® Magnetic	ChromoTek	discontinued
GFP-Trap® Magnetic Agarose	ChromoTek	Cat# gtma-10
Glutathione Sepharose 4 Fast Flow	GE Healthcare	Cat# GE17-5132-01
Ni-NTA Agarose	QIAGEN	Cat# 30250
Anti-HA Magnetic Beads	Thermo Scientific	Cat# 88837
BCA Protein Assay Kit	Thermo Scientific	Cat# 23225
Cytiva Amersham™ Hyperfilm ECL	Thermo Scientific	Cat# 10607665

(*Continued on next page*)

Continued

REAGENT or RESOURCE	SOURCE	IDENTIFIER
Deposited Data		
Structured data for Ede1 (1220-1247) peptide-Atg8^{K26P}	This study	PDB: 6WY6
Proteomics (ProteomeXchange Consortium)	This study; PRIDE Dataset	PXD019083
Original western blot, Coomassie stained images, and microscopy images	This study; Mendeley Dataset	https://doi.org/10.17632/ghmnt5jm73.1
Experimental Models: Organisms/Strains		
S. cerevisiae DF5, see Table S2	Ulrich and Jentsch, 2000	N/A
Recombinant DNA		
Plasmid: pGEX-4T3, see Table S3	This study	N/A
pRS414-pMet17-2xmCherry-Atg8	This study	N/A
YCplac33-yeGFP-Atg8	This study	N/A
YCplac33-yeGFP	This study	N/A
pGEX-2TK-GST-Atg8	This study	N/A
p415 ADH-2 × HA-Atg8	This study	N/A
Plasmid: YIplac211, see Table S3	This study	N/A
pET28a-Atg8	This study	N/A
Software and Algorithms		
Perseus (version 1.5.4.2)	Tyanova et al., 2016	https://maxquant.net/perseus/
Image Studio	LI-COR Biosciences	https://www.licor.com/bio/image-studio/?gclid=EAIaIQobChMInO7ihc224wIVSxbTCh3irwQdEAAYASAAEgLj8fD_BwE
GENEONTOLOGY (GO)	Ashburner et al., 2000	http://geneontology.org
iLIR	Kalvari et al., 2014	http://repeat.biol.ucy.ac.cy/iLIR/
LCR-eXXXplorer	Kirmitzoglou and Promponas, 2015	http://repeat.biol.ucy.ac.cy/fgb2/gbrowse/swissprot/
Phenix	Liebschner et al., 2019	https://www.phenix-online.org/
STRING	Szklarczyk et al., 2019	https://string-db.org/
Coot	Emsley and Cowtan, 2004; Emsley et al., 2010	https://www2.mrc-lmb.cam.ac.uk/personal/pemsley/coot/
CCP4 (CCP-EM)	Burnley et al., 2017	http://www.ccpem.ac.uk/download.php
HKL2000	Otwinowski and Minor, 1997	https://hkl-xray.com/download-instructions-hkl-2000
SoftWoRx® Software	GE Healthcare	http://incelldownload.gehealthcare.com/bin/download_data/SoftWoRx/7.0.0/SoftWoRx.htm
ImageJ/Fiji	Schindelin et al., 2012	https://imagej.net/Fiji
YeastSpotter	Lu et al., 2019	http://yeastspotter.csb.utoronto.ca/
Cellprofiler (version 2.2.0)	Carpenter et al., 2006; Jones et al., 2008	https://cellprofiler.org/
SerialEM	Mastronarde, 2005	http://bio3d.colorado.edu/SerialEM/
MATLAB (2018a)	MathWorks	https://www.mathworks.com/
IMOD	Kremer et al., 1996	http://bio3d.colorado.edu/imod/
PyTom	Hrabe et al., 2012	http://strubi.chem.uu.nl/pytom/
CTFFIND 4.1.5	Rohou and Grigorieff, 2015	https://grigoriefflab.umassmed.edu/ctf_estimation_ctffind_ctftilt
Prism 8.4.3	GraphPad	https://www.graphpad.com/scientific-software/prism/

RESOURCE AVAILABILITY

Lead Contact

Further information and requests for resources and reagents should be directed to and will be fulfilled by the Lead Contact, Florian Wilfling (fwilfling@biochem.mpg.de).

Materials Availability

All unique reagents generated in this study are available from the Lead Contact without restriction or require a completed Materials Transfer Agreement if there is potential for commercial application.

Data and Code Availability

The mass spectrometry proteomics raw data have been deposited to the ProteomeXchange Consortium through the PRIDE partner repository with the dataset identifier PXD019083. The coordinate and structure factors for Ede1-Atg8 were deposited to the RCSB Protein Data Bank with ID 6WY6. Original data have been deposited to Mendeley Data: https://doi.org/10.17632/ghmnt5jm73.1.

EXPERIMENTAL MODEL AND SUBJECT DETAILS

Yeast Cell Culture, Starvation, GFP Cleavage Assay, Spotting Assay and Cloning

All strains used in this study are derivatives of *Saccharomyces cerevisiae* and are listed in Table S2. Standard protocols for transformation, mating, sporulation, and tetrad dissection were used for yeast manipulations (Dunham et al., 2015). Yeast cultures were inoculated from overnight cultures, grown using standard growth conditions and media (Sherman, 2002). If not indicated otherwise, cells were cultured at 30°C in YPD-medium (1% yeast extract, 2% peptone and 2% glucose). For GFP cleavage assay, cells were grown to mid-log phase (optical density at 600 nm (OD_{600}) of 1.0) then switched into SD-N medium (synthetic minimal medium lacking nitrogen; 0.17% YNB without amino acids and ammonium sulfate, supplemented with 2% glucose) and incubated for the indicated time. Alternatively, cells were treated with 100 nM rapamycin for the indicated times. Mitophagy was examined as described previously (Tal et al., 2007). Autophagy substrates were tagged at the endogenous, chromosomal location with EGFP and their vacuolar degradation following starvation was monitored by accumulation of the released EGFP moiety, which is largely resistant to vacuolar degradation. For spotting growth assay, 5×10^4 cells from overnight cultures were 5-fold serially diluted and dropped onto YPD plates. Plates were scanned after an incubation for 3 days at 30°C. Chromosomally tagged strains and knockout strains were constructed by a PCR-based integration strategy (Knop et al., 1999). Standard cloning and site-directed mutagenesis techniques were used to generate the described plasmids (Table S3).

METHOD DETAILS

Immunoblot Techniques

Yeast protein extraction was performed as described before (Cheong and Klionsky, 2008). In short, the TCA (Trichloroacetic acid; to a final concentration of 10% for 20 min on ice) precipitated cell pellet was resuspended in 100 µl MURB buffer (50 mM Na_2HPO_4, 25 mM 2-[N-morpholino]ethanesulfonicacid (MES), pH 7.0, 1% SDS, 3 M urea, 0.5% 2-mercaptoethanol, 1 mM NaN_3 and 0.05% bromphenol blue) and disrupted by vortexing with an equal volume of acid-washed glass beads for 5 min. Followed by an incubation at 70°C (1400 rpm) for 10 min. For detection of biotinylation on the acceptor peptide tagged-proteins 10 µg of Streptavidin (2 mg/ml) was added to the MURB buffer resuspended sample. Proteins were separated by NuPAGE™ Novex™ 4%–12% gradient or 12% Bis-Tris-protein gels (Invitrogen), transferred onto PVDF membranes (Immobilon®-P) and then analyzed using specific antibodies (see Key Resources Table) and imaging with an Odyssey® Fc imager (LI-COR) or classical film development. For quantification performed with the Odyssey® Fc imager (LI-COR), proteins were transferred onto low fluorescence PVDF membranes (Immobilon®-FL), and analyzed using specific antibodies followed by fluorescent IRDye® secondary antibodies.

Co-immunoprecipitation

Yeast cell lysates from 200 OD_{600} were prepared by cell disruption on a multitube bead-beater (MM301 from Retsch GmbH) in lysis buffer (100 mM HEPES pH 7.4, 150 mM NaCl, 1% NP-40, 10% glycerol, 50 mM NaF, 2 mM phenylmethylsulfonyl fluoride (PMSF), and EDTA-free protease inhibitor cocktail (cOmplete Tablets, Roche)) with zirconia/silica beads. The extracts were cleared by centrifugation at 8000 g for 10 min and supernatants were incubated with GFP-Trap_A matrix (ChromoTek) or anti-HA magnetic beads (Thermo Scientific) for 2 h with head-over-tail rotation at 4°C and followed by 5 times washing steps with lysis buffer to remove nonspecific background binding. Bound proteins were eluted by adding HU loading buffer and incubation at 65°C for 10 min.

Mass Spectrometry and Data Analysis

To analyze the Atg8 interactome for the different yeast strains, four biological replicates of cells were grown at 30°C in 200 mL YPD medium each. At OD_{600} 1.0, cells were incubated for 3 h with 100 nM rapamycin. Yeast cells were subsequently collected by centrifugation and lysates were prepared by cell disruption on a multitube bead-beater (MM301 from Retsch GmbH) in lysis buffer (20 mM

HEPES pH 7.5, 150 mM KOAc, 1% NP-40, 5% glycerol, 10 mM N-Ethylmaleimide, 1 mg/ml Pefabloc SC (Roche), and EDTA-free protease inhibitor cocktail (cOmplete Tablets, Roche)) with zirconia/silica beads. The extracts were cleared by centrifugation at 2000 g for 10 min. Supernatants were incubated with GFP-Trap_M or GFP-Trap_MA matrix (ChromoTek GmbH) for 1 h on a rotary wheel at 4°C. Magnetic beads were washed 2 times with lysis buffer and 4 times with washing buffer (50 mM Tris pH 7.5, 150 mM NaCl, 1 mg/ml Pefabloc SC (Roche), and EDTA-free protease inhibitor cocktail (cOmplete Tablets, Roche)) to remove any residual detergent. The supernatants from the beads were removed and the beads were incubated with a buffer containing 4 M urea and 20 mM DTT in 25 mM Tris pH 8.0 buffer for 10 minutes followed by incubation with 40 mM chloroacetamide for 20 minutes for alkylation of cysteines. The sample was diluted to final concentration of 1 M urea with digestion buffer (25 mM Tris pH 8.0) and vortexed. The sample was digested for 2 h with 0.5 μg of endoproteinase lysine-C (Wako chemicals) and then digested with 0.5 μg of trypsin (Promega) overnight. The digested peptides were purified using StageTip (Rappsilber et al., 2003). Peptides were loaded on a 15 cm column (inner diameter = 75 microns) packed with C18 reprosil three-micron beads (Dr Maisch GmbH) and directly sprayed into a LTQ-Orbitrap XL instrument operated in a data-dependent fashion. Up to top five precursors were selected for fragmentation by CID and analyzed in the iontrap. The raw data were processed using MaxQuant (Cox and Mann, 2008) version 1.6.0.15. Peak lists generated were searched against a yeast ORF database using Andromeda search engine (Cox and Mann, 2008) built into Maxquant. Proteins were quantified using the MaxLFQ algorithm (Cox et al., 2014). Analysis was performed using Perseus (Tyanova et al., 2016) version 1.5.4.2 as described before (Hubner et al., 2010). The mass spectrometry proteomics data have been deposited to the ProteomeXchange Consortium via the PRIDE (Perez-Riverol et al., 2019) partner repository with the dataset identifier PXD019083.

Protein Sample Production for Crystallography

S. cerevisiae Atg8 (1-116) with stabilizing mutation K26P was expressed from pGEX-4T-1 vector in BL21 gold *E. Coli* strain. Transformed culture was grown at 37°C to OD_{600} 0.8, and then induced at 18°C by addition of 0.6 mM IPTG (final concentration) for 12 hours. Cells were collected by centrifugation, re-suspended, and lysed by sonication in a buffer containing 25 mM Tris–HCl pH 7.6, 200 mM NaCl, 5 mM DTT. The cell lysate was clarified by high-speed centrifugation at 15,000 rpm. Atg8 protein was extracted from the resulting supernatant through affinity pull-down purification using glutathione Sepharose 4B resin (GE now Cytiva), and cleaved by thrombin incubation on resin in the same buffer. Untagged Atg8 was purified by cation ion exchange chromatography on HiTrap SP HP column (GE now Cytiva) in buffers containing 25 mM HEPES pH 7.0, 1 M NaCl and 5 mM DTT (buffer A) and 25 mM HEPES 7.0 and 5 mM DTT (buffer B). After ion exchange, Atg8 was further purified by size exclusion chromatography using Superdex 200 column (GE now Cytiva) in a buffer containing 25 mM Tris–HCl pH 7.6, 200 mM NaCl, 5 mM DTT. The purification steps of Atg8 described above follow the same production protocol as described for human LC3 (Zheng et al., 2017b). Atg8 protein was mixed with HPLC-purified synthetic Ede1 (1220-1247) peptide at a molar ratio of 1:2, followed by a 5-minute incubation at 4°C. The complex was purified by size-exclusion chromatography using Superdex75 10/300 GL (Sigma) column in buffer containing 20 mM HEPES (pH 7.0), 100 mM NaCl, and 5 mM DTT. The peak fractions were concentrated to 33 mg/ml as the final sample.

Crystallization of Ede1-Atg8 Complex

Crystals were obtained using vapor diffusion method with macro seeding procedure for improvement. 1 μl of protein was mixed with 1 μl of well buffer containing 1.3 M ammonium sulfate and 0.1 M sodium acetate (pH 4.8), and was allowed to grow in hanging drops at 4°C for 24 h. The resulting crystals were crushed and diluted in the same well buffer to be used as seeds. Final crystals were obtained by mixing 0.2 μl seeds, 1 μl of protein sample, and 1 μl of well buffer containing 1.1 M ammonium sulfate, 0.1 M sodium acetate (pH 4.8), and 0.01 M sodium iodide after growth at 4°C for 48 - 72 h in hanging drops before harvest. Crystals were cryo-protected in 25% glycerol in addition to the mother liquor, and were flash-frozen in liquid nitrogen 48 h prior to the data collection.

Data Collection, Processing, Refinement and Deposition

Data for Ede1-Atg8 complex was collected at Advanced Photon Source (APS) SER-CAT beamline 22-BM. Use of the Advanced Photon Source was supported by the U. S. Department of Energy, Office of Science, Office of Basic Energy Sciences, under Contract No. W-31-109-Eng-38. The dataset was created from a single crystal, and was processed and scaled by HKL2000. Phase was solved by molecular replacement using Phaser in CCP4, adopting Atg19-Atg8 complex structure (PDB: 2ZNP) as search model. Model was built in Coot. And refinements were primarily performed by Refmac in CCP4, and finalized by Refmac in Phenix. The coordinate and structure factors for Ede1-Atg8 were deposited to the RCSB Protein Data Bank with ID 6WY6.

Expression and Purification of GST-fusion Proteins and His-Atg8

GST-fusion proteins and His-Atg8 were expressed in *E. coli* Rosetta™ 2(DE3) (for GST-fusion proteins) or Rosetta™ 2(DE3)pLysS (for His-Atg8) cells, respectively. Expression was induced with 1 mM IPTG in a 1 L culture of LB (lysogeny broth) for 20 h at 22°C. Cells were harvested by centrifugation and lysed in lysis buffer (GST-fusion proteins: 40 mM Tris pH 7.5, 150 mM NaCl, 5 mM DTT, EDTA-free protease inhibitors cocktail (cOmplete Tablets, Roche), 1 mg/ml Pefabloc SC (Roche); His-Atg8: 40 mM Tris pH 7.5, 500 mM NaCl, 5 mM $MgCl_2$, 5 mM 2-Mercaptoethanol, 20 mM Imidazole, 10% glycerol (w/v), EDTA-free protease inhibitors cocktail (cOmplete Tablets, Roche), 1 mg/ml Pefabloc SC (Roche)) using an EmulsiFlex C3 homogenizer (Avestin). DNA was digested using SM DNase (final 75 U/ml, 15 min on ice). Supernatant containing soluble proteins was collected by centrifugation (20000 rpm, 30 min). GST-fusion proteins and His-Atg8 were affinity purified using Glutathione Sepharose 4 Fast Flow (GE Healthcare) or Ni-NTA

agarose (QIAGEN) respectively (2.5 h on a rotary wheel at 4°C). The resins were recovered by gravity-flow chromatography. Resins were subsequently washed 3 times with 25 mL lysis buffer, followed by 3 times with washing buffer (GST-fusion proteins: 40 mM Tris pH 7.5, 450 mM NaCl, 5 mM DTT; His-Atg8: 40 mM Tris pH 7.5, 500 mM NaCl, 5 mM $MgCl_2$, 5 mM 2-Mercaptoethanol, 70 mM Imidazole, 10% glycerol (w/v)). Bound proteins were eluted from the individual resin (GST-fusion proteins: 40 mM Tris pH 7.5, 150 mM NaCl, 5 mM DTT, 50 mM glutathione; His-Atg8: 40 mM Tris pH 7.5, 500 mM NaCl, 5 mM $MgCl_2$, 5 mM 2-Mercaptoethanol, 270 mM Imidazole, 10% glycerol (w/v)). The eluted proteins were collected and dialyzed (50 mM Tris pH 7.5, 150 mM NaCl, 20% glycerol (w/v), overnight 4°C). Purified proteins were directly frozen after dialysis and stored in aliquots at −80°C until further use. The identity of the different proteins was confirmed by SDS-PAGE. Protein concentration was determined by Pierce™ BCA protein assay kit.

Atg8 *In Vitro* Binding Assay

The *in vitro* binding assay was performed by incubation of the indicated protein combinations in 1 mL assay buffer (50 mM Tris pH 7.5, 150 mM NaCl, 5% glycerol (w/v), 20 mM Imidazol, 0.1% Triton X-100) for 1 h at room temperature. 50 µl were used as input control and mixed with an equal amount of HU loading buffer (8 M Urea, 5% SDS, 200 mM Tris-HCl pH 6.8, 20 mM dithiothreitol (DTT), and Bromophenol blue 1.5 mM). The rest of the supernatant was added to 100 µl Ni-NTA agarose (QIAGEN) slurry and incubated for 2.5 h at 4°C on a rotary wheel. The resin was collected by centrifugation (800 rpm, 1 min) and washed 6 times with 1 mL washing buffer (50 mM Tris pH 7.5, 150 mM NaCl, 5% glycerol (w/v), 20 mM Imidazol, 1% Triton X-100). After the last washing step, the supernatant was removed (27G needle) and the proteins were eluted with 50 µl of elution buffer (50 mM Tris pH 7.5, 150 mM NaCl, 5% glycerol (w/v), 270 mM Imidazol, 1% Triton X-100). The eluate was transferred into a new tube (27G needle), mixed with an equal amount of HU loading buffer and analyzed by SDS-PAGE. Proteins separated by SDS-PAGE were stained with PageBlue Protein Staining Solution (Thermo Scientific).

GST-Atg8 Pulldown with Yeast Cell Extract

The indicated GST-fusion proteins were incubated (3 nM) diluted in 1 mL assay buffer (50 mM Tris pH 7.5, 150 mM NaCl, 5% glycerol (w/v, 0.1% Triton X-100) and mixed with 50 µl Glutathione Sepharose 4 Fast Flow (GE Healthcare) slurry. The mixture was incubated for 2.5 h at 4°C on a rotary wheel. Meanwhile, the yeast lysate was prepared as described above (mass spectrometry, 20 µl were kept as input control and mixed with 200 µl HU loading buffer). The Glutathione Sepharose was collected by centrifugation (800 rpm, 1 min) and washed one time with washing buffer (50 mM Tris pH 7.5, 150 mM NaCl, 5% glycerol (w/v), 1% Triton X-100) followed by one time with the yeast lysis buffer (20 mM HEPES pH 7.5, 150 mM KOAc, 1% NP-40, 5% glycerol, 1 mg/ml Pefabloc SC (Roche), and EDTA-free protease inhibitor cocktail (cOmplete Tablets, Roche)). Subsequently, 300 µl of the yeast lysate was mixed with 700 µl yeast lysis buffer and added to the resin (2.5 h, 4°C rotary wheel). The resin was washed three times with yeast lysis buffer and the supernatant was in the final step removed with a 27G needle. The bound proteins were denatured by addition of 50 µl HU loading buffer and incubation at 65°C for 10 min.

Fluorescence Microscopy

For fluorescence microscopy, yeast cells were grown in low fluorescence synthetic growth medium (yeast nitrogen base without amino acids and without folic acid and riboflavin (FORMEDIUM)) supplemented with all essential amino acids and 2% glucose. The next day cells were diluted to OD_{600} 0.1 and grown till mid log phase (0.5 – 0.8 OD_{600}) before imaged. Microscopy slides were pre-treated with 1 mg/ml Concanavalin A (ConA) solution. The widefield imaging was performed at the Imaging Facility of the Max Planck Institute of Biochemistry (MPIB-IF) on a GE DeltaVision Elite system based on an OLYMPUS IX-71 inverted microscope, an OLYMPUS (100X/1.40 UPLSAPO or 60X/1.42 PLAPON) objective and a PCO sCMOS 5.5 camera. Images were deconvolved using the softWoRx® Software (default values except: method: additive enhanced, 20 iterations). Image analysis was performed using ImageJ/Fiji (Schindelin et al., 2012; Schneider et al., 2012).

FRAP and FLIP Analysis

For FRAP analysis 131 frames were collected with a time interval of 1 s. 10 frames were collected before bleaching with a high laser power (point bleaching) for 1 frame. 120 frames were collected after bleaching. Double normalization or single normalization was performed (Phair et al., 2004). For this the average fluorescence intensities were recorded within the bleached region, the total END compartment and a random region outside of the cell for background subtraction before and immediately after photobleaching. In comparison to the single normalization method double normalization involves normalization of the recovery signal to the average prebleach signal and, at the same time, takes into account the loss of total signal due to the bleach pulse and bleaching during subsequent imaging. Fitting of normalized FRAP curves was performed using a single exponential equation with the software Origin (version 2019b). FLIP analysis was performed as described before (Snapp, 2013).

Yeast Spot Analysis

Quantification of fluorescent spots in yeast cells was performed using the software ImageJ/Fiji (Schindelin et al., 2012; Schneider et al., 2012), complemented with the plugins provided by the ImageScience update site. Cells in each image were identified with YeastSpotter (Lu et al., 2019), which was installed locally and controlled through Fiji. The workflow was implemented as a series

of actions in an ImageJ Toolset, each action performing a processing step on all the images in a given directory. As a first step, the stacks of fluorescent images acquired were compressed by maximum intensity projection. YeastSpotter was then executed on DIC (Differential Inference Contrast) images from the same field of view, to generate a mask identifying position and size of cells, to apply to the corresponding fluorescence image. In order to eliminate possible detection errors, the candidate cells were screened for diameter (larger than 4 μm) and aspect ratio (smaller than 5). Each cell was analyzed independently, with their spots being first enhanced with a Laplacian of Gaussian operator (FeatureJ: Laplacian plugin, smoothing scale 63 nm) and then detected by thresholding. The threshold was set adaptively to 9 times the standard deviation above the average intensity of the cell. In order to avoid that the average intensity was biased by the strength and number of spots, this one was calculated after excluding all the pixels with intensity 3 times the standard deviation above an initial estimate from all the pixels in the cell.

Microfluidics Experiments

Microfluidics experiments were performed on a CellASIC® ONIX microfluidic platform (Merck) with the CellASIC® ONIX microfluidic plates for haploid yeast cells. To test the impact of 1-,6-Hexanediol on proteins of END, WT or *ΔΔΔ* mutant cells with endogenously tagged Ede1-EGFP were loaded from a logarithmic growing culture (OD_{600} 0.5 – 0.8) according to manufacturer's manual and imaged in 12 s intervals over a time course of 26 min. At each position for each time point a midplane image was recorded. Imaging was performed at a constant media flow rate of 1 psi. After 2 min the media stream was switched from low fluorescence synthetic growth medium to low fluorescence synthetic growth medium containing 10% 1-,6-Hexanediol and 10 μg/ml digitonin (Sigma). Cells were perfused for 3 min before the media stream was switched back to the regular low fluorescence synthetic growth medium. For monitoring END degradation cells were loaded from a logarithmic growing culture (OD_{600} 0.5 – 0.8) according to manufacturer's manual and imaged in 8 min intervals over a time course of 8 h. At each position for each time point a z stack was recorded (300 nm). Imaging was performed at a constant media flow rate of 1 psi. To rapidly switch media, flow rate was set to 5 psi for 5 min and then switched back to a flow rate of 1 psi. Cells were initially cultured in low fluorescence synthetic growth medium and then switched to SD-N medium. The microscope used was the same as described in the Fluorescence Microscopy section.

Automated Yeast Library Manipulations and High-throughput Microscopy

All genetic manipulations were performed using Synthetic Genetic Array (SGA) techniques to allow efficient introduction of the eGPF-tagged *EDE1* locus under the control of the *ADH* promoter into a systematic yeast knockout library (Thermo Fisher). SGA was performed as previously described (Collins et al., 2010; Tong and Boone, 2006). Briefly, using a Biomek FXP (Beckman Coulter) to manipulate libraries in 384-colony high-density formats, haploid strains from opposing mating types, each harboring a different genomic alteration, were mated on rich media plates. Diploid cells were selected on plates containing all selection markers found on both parent haploid strains. Sporulation was than induced by transferring cells to plates containing 1% potassium acetate. Haploid cells containing all desired mutations were selected for by transferring cells to plates containing all selection markers alongside the toxic amino acid derivatives Canavanine and Thialysine (Sigma-Aldrich) to select against remaining diploids. Microscopic screening was performed using an automated microscopy set-up, using an Opera Phenix high content screening system (PerkinElmer). Images were acquired using a 60X water lens with excitation at 490/20 nm and emission at 535/50 nm (GFP). After acquisition at basal (YPD medium) and starvation-induced growth condition (24 h SD-N medium), images were analyzed and manually reviewed using the Harmonie 4.8 software for the visual analysis of END compartment or Cellprofiler 2.2 and MATLAB 2018a for analysis of colony growth. Each strain was generated in duplicates. For the visual screen 4 images per strain were acquired. Images were analyzed by defining the number of END spots per image divided by the total cell area. A z-score for each individual value against the screen mean was computed. Table S1 shows hits with a z-score higher then 1.5.

Electron Microscopy

Cryo-EM sample preparation

For cryo-ET experiments, yeast cultures were inoculated from overnight cultures and grown in YPD media at 30°C to an OD_{600} of 0.6. To allow for later 3D-correlation, cells were supplemented with fiducial markers (Dynabeads MyOne, Thermo Fisher Scientific) at 1:16 dilution. The cell suspension containing fiducials (4 μL) was applied to holey carbon R2/1 copper, or holey SiO_2 R1/4 TEM grids (Quantifoil) to allow for more robust correlation and cells were plunge frozen on a Vitrobot Mark IV (FEI, settings: blotforce = 10, blottime = 10 s, temperature = 30°C, humidity = 90%). Samples were stored under LN_2 until use. Grids containing vitrified yeast cells were clipped in modified Autogrids, and fluorescent image stacks (typically 70 slices at 300 nm steps) were recorded in confocal mode at selected squares using a 40x long distance air objective (Zeiss EC Plan-Neofluar 40x/0.9 NA Pol) on a fluorescence microscope equipped with a cryo module (Corrsight, FEI) using the 488 laser channel. Potential sites of Ede1 accumulation were identified in the FLM stacks and correlated using custom software (Arnold et al., 2016) with the SEM/IB images of a dual beam focused ion beam microscope (FIB Quanta 3D FEG, FEI) equipped with a Quorum PP3000T cryo-system (Quorum Technologies, Laughton, United Kingdom) and a homemade 360° cryo-stage cooled by an open nitrogen circuit (Rigort et al., 2010). Lamellas were cut at correlated sites analogous to published protocols (Schaffer et al., 2017).

Cryo-EM data acquisition

Cryo-tomograms were acquired on a transmission electron microscope (Titan Krios, FEG 300 kV, FEI) with a post-column energy-filter (968 Quantum K2, Gatan) with a defocus range of −5 μm to −3.5 μm and an EFTEM magnification of 42000x (calibrated pixel size

3.42 Å). Images were recorded with a direct detection camera (K2 Summit, Gatan) in dose-fractionation mode and a total dose of ~140 e^- / $Å^2$ per tomogram using the SerialEM software package (Mastronarde, 2005). The acquisition was controlled by an in-house script running a dose-symmetric tilt scheme (Hagen et al., 2017) with an angle increment of 2° between the range of 70° and −50° starting at 10° to compensate for the lamella pre-tilt (~12°). Frames were aligned using motioncorr2 (Zheng et al., 2017a), and tilt-series alignment as well as tomogram reconstruction was performed in IMOD (Kremer et al., 1996).

Cryo-EM template matching and subtomogram averaging

Ribosome positions were determined by template matching on 2x binned tomograms (IMOD bin 4, 13.68 Å pixel size) using the PyTom (Hrabe et al., 2012) software package. A reference was constructed from ~300 manually picked ribosomes, which were aligned in PyTom using a fast-rotational matching (FRM) algorithm. The reference was further truncated at the small subunit to allow removal of false positives. For each tomogram, the 600 highest scoring cross-correlation peaks were extracted, and the subtomograms aligned (FRM) and classified using constrained principal component analysis (CPCA) to remove false positives as judged by the absent small subunit in the class averages. After initial processing in PyTom, further classification and refinement of the unbinned subtomogram averages was performed in Relion 2.1 (Scheres, 2012), including normalization and CTF estimation with CTFFIND 4.1.5 (Rohou and Grigorieff, 2015). The final list of particles (~11000) yielded a ribosome structure at 16 Å resolution (0.143 FSC criterion), which was used in all animations with appropriate binning.

Visualization

To enhance the contrast of TEM insets, the sum projections of 5 slices each around a central slice are shown. For 3D visualization, membranes were manually segmented in AMIRA 6.2 (FEI) and subtomogram averages of ribosomes (2x binned) were placed at positions derived from template-matching and cleaned by classification using custom MATLAB (Mathworks) scripts. Static scenes and videos were rendered in Chimera (Pettersen et al., 2004) at 13.68 Å pixel size (bin 2x).

Isothermal Titration Calorimetry (ITC)

All the ITC measurements were carried out in MicroCal PEAQ-ITC at 25°C. Atg8 was purified via GST affinity chromatography followed by size exclusion chromatography in final buffer containing 25 mM Tris-HCl at pH 7.5, 150 mM NaCl and 0.5 mM TCEP. The Ede1 peptide, ADSESEFENVANAGSMEQFETIDHKDLDW used for the experiments was synthesized in the biochemistry core facility of the MPIB and diluted in the same buffer as the protein for the ITC experiments. Experiments were carried out with settings of 18 injections of 2 μl with 150 s injection spacing in between, 4 s injection duration and reference power of 10 μcal/s. Measurements were carried out by titrating the protein with final concentration of 280-339 μM into the peptide at 20 μM. The final ITC data were analyzed using one site binding model and final plots were made using GraphPad Prism.

QUANTIFICATION AND STATISTICAL ANALYSIS

Error bars represent SD as indicated in the figure legends. Data were processed in Prism. Statistical analysis of differences between two groups was performed using a two-tailed, unpaired t test.